ROYAL SOCIETY
OF CHEMISTRY

REVIEW

Check for updates

Recent progress in layered metal dichalcogenide nanostructures as electrodes for high-performance sodium-ion batteries

Wenpei Kang,[a] Yuyu Wang[a] and Jun Xu (ID) *[b]

Sodium-ion batteries (SIBs) have emerged as a promising candidate for large-scale stationary energy storage in light of possible concerns over cost and abundance. Advanced sodium host materials are required for developing SIBs with high energy density, long cycling stability and high safety. Layered metal dichalcogenides (MX_2, M = Mo, W, Sn, V, Ti; X = S, Se, Te) have become a hot spot for anode materials in SIBs due to their merits of high conductivity, mechanical and thermal stability and structural stability. In this review, we first present a comprehensive overview of the progress of layered MX_2 anodes for SIBs. Detailed discussion on the advantages of MX_2 as SIB anodes is then made. Emphasis is placed on enhancing the electrochemical performance through nanostructure engineering, crystal structure modulation, doping/alloying and composite design. We conclude with a perspective on the further development of SIBs in view of their applications.

1. Introduction

Nowadays renewable and sustainable resources (*e.g.*, solar and wind) have attracted worldwide attention attributed to increasing environmental problems and energy crisis originating from traditional fossil fuels. But these renewable resources are always intermittent and affected by weather and geographical regions, for which energy storage systems (ESSs)

play a key role in their better utilization.[1–6] Battery tools have been regarded as appropriate ESSs because of their high conversion efficiency and the advantages of long cycle life and relatively low maintenance.[7–12] Over the past two decades, lithium-ion batteries (LIBs) have developed rapidly since their first commercialization by Sony in 1991, and have been widely used to power portable devices such as laptops, cell phones and power tools for electric vehicles (EVs) and hybrid electric vehicles (HEVs).[13–17] On the other hand, dramatic developments in large-scale ESSs for smart grids will require substantially greater amounts of materials to build secondary batteries. As a result,

[a]State Key Laboratory of Heavy Oil Processing, College of Science, China University of Petroleum (East China), Qingdao 266580, P. R. China

[b]School of Electronic Science & Applied Physics, Hefei University of Technology, Hefei 230009, P. R. China. E-mail: apjunxu@hfut.edu.cn

Wenpei Kang obtained her Ph.D. degree in Physical Chemistry from Shandong University in 2013, and then moved to the Center Of Super Diamond and Advanced Films (COSDAF) at the City University of Hong Kong as a senior research assistant working on rechargeable battery electrode materials. She joined China University of Petroleum (East China) in 2016, and works as an associate professor in College of Science. Her research interest includes synthesis and application of materials for electrochemical energy storage and conversion systems.

Yuyu Wang received her bachelors degree in Chemistry from Ludong University in 2016. She is currently a postgraduate student under the supervision of Dr Wenpei Kang in College of Science, China University of Petroleum (East China). Her research focuses on MOF-derived materials for lithium and sodium ion batteries.

basic factors including energy density, power density, cost, life and safety need to be well balanced for secondary batteries.[18–21]

Li cannot be regarded as an abundant element because of its low mass fraction ($\sim$20 ppm) in the earth's crust, resulting in the continuous increase in the cost of LIBs based on the high demand for Li-based raw materials.[22–24] In contrast, Na is abundant with a lower price and is the second lightest and smallest alkali metal next to Li, which make sodium-ion batteries (SIBs) show great superiority when a large amount of raw materials are required in large-scale ESSs.[25–30] In addition, owing to the similar electrochemistry behavior between Li and Na, the state-of-art advances in LIBs may be extended to develop SIBs. In fact, reversible electrochemical insertion of sodium has been demonstrated in the 1980s.[31] The electrochemical properties of sodium-containing layered oxides (Na_xCoO_2) were reported at almost the same time when the cathode material $LiCoO_2$ widely used in most commercial LIBs was first reported.[32,33] However, SIBs were neglected for practical applications due to their inferior performance for a long time. Several obstacles need to be overcome before SIBs can be practically and commercially applied, since Na^+ ions are $\sim$34% larger in radius than Li^+ ions (1.02 Å for Na^+ ion vs. 0.76 Å for Li^+ ion). As a result, it is highly desirable to explore suitable host materials to accommodate Na^+ ions and facilitate reversible insertion–extraction of Na^+ ions.[34–45]

In the past few years, high demands for and large-scale applications of secondary batteries have promoted the rapid development of ambient-temperature SIBs. Plenty of cathodes, anodes and electrolytes for SIBs have been studied. It is generally known that anodes in secondary batteries determine some key characteristics, such as safety and cycling life. Thus, it is indispensable to find suitable anode materials for SIBs. Graphite, employed as the commercial anode for LIBs, cannot function well in SIBs due to its extremely low capacity and poor kinetics.[46–48] Therefore, numerous attempts have been made to explore suitable anodes for SIBs. Recent findings have shown that alloy-type[49–54] and conversion-type[55–58] anode materials can exhibit impressive initial capacity, but the cyclability is poor due to the large volume change and the limited kinetics. In addition, some non-graphitic carbon (e.g., hard carbon and carbon

spheres),[59–61] organic-based anode materials,[62,63] carbide[64] and titanium-based intercalation compounds[65,66] have also been investigated as anode materials for SIBs with limited reversible capacities of 100–300 mA h g^{-1}.

Transition metal sulfides based on conversion or alloying reactions have been explored and evaluated as anode materials for LIBs.[58,67–70] Recently, these materials have also attracted extensive attention for their applications as high capacity anodes that may boost the high energy density of SIBs.[26,27,29,44,71–73] Among them, layered metal dichalcogenides (MX_2, M = Mo, W, Sn, V, Ti; X = S, Se, Te) with similar layered structures to graphite exhibited better cycling performance than other transition metal sulfides. When these layered MX_2 compounds consist of single- or few-layered structures, they belong to the two dimensional (2D) family.[74–76] Each slab in MX_2 consists of a hexagonally close-packed sheet of metal atoms (M) sandwiched between the two sheets of chalcogen atoms (X). While the intraslab M–X bonds are covalent, the MX_2 slabs are stacked by van der Waals forces similar to the graphene layers in graphite. Representative crystal structures, interlayer spacing and the theoretical capacities are shown in Fig. 1. Typically, MX_2 has a larger interlayer spacing (e.g., $\sim$6.15 Å for MoS_2) than graphite (3.3 Å), providing large channels for Na^+ ion intercalation. The enlarged interlayer can well accommodate volumetric expansion upon sodium storage and mitigate the strain endured in the intercalation or conversion reaction, leading to enhanced cycling stability, which makes it attractive in view of a practical battery design. MX_2 nanosheets and their hierarchical organization are promising electrode candidates for SIBs because of their unique physical and chemical properties, such as conductivity, mechanical and thermal stability, and cyclability. Nevertheless, properly designed nanostructure MX_2 may reduce diffusion/transport lengths for both ions and electrons, increase active sites, and further relieve the volume expansion/contraction, thus leading to increased capacity, higher power/energy density, and improved cycling life (Table 1). Therefore, an up-to-date and comprehensive account of the current status and challenges of MX_2 as advanced SIB electrode materials is highly desirable.

In this review, we present a summary of the synthesis, modification, and electrochemical performance of nanostructured layered MX_2. In particular, their sodium storage applications are emphasized. The relationship between nanoarchitectures and electrochemical performances as well as related sodium storage mechanisms is discussed. More research work is required for practical applications of layered MX_2 electrodes in the coming future.

2. Nanostructured MoX_2 electrode materials for SIBs

2.1 MoS_2 electrodes

MoX_2 (X = S, Se, Te) nanosheets exhibit a remarkably diverse range of unique optical, electrochemical, and mechanical properties.[77–82] They have been widely used as functional materials in diverse fields of lubrication, electronic transistors,
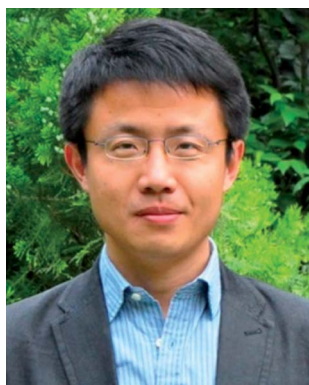
Jun Xu obtained his Ph.D. degree in physics and materials science from the City University of Hong Kong (CityU) in 2012, and then continued as a senior research associate at the Center Of Super-Diamond and Advanced Films (COSDAF), CityU. He joined Hefei University of Technology in 2013, and works as a professor in the School of Electronic Science and Applied Physics. His research interest focuses on inorganic nanomaterials, electrochemical and photoelectrochemical devices, and solar cells.
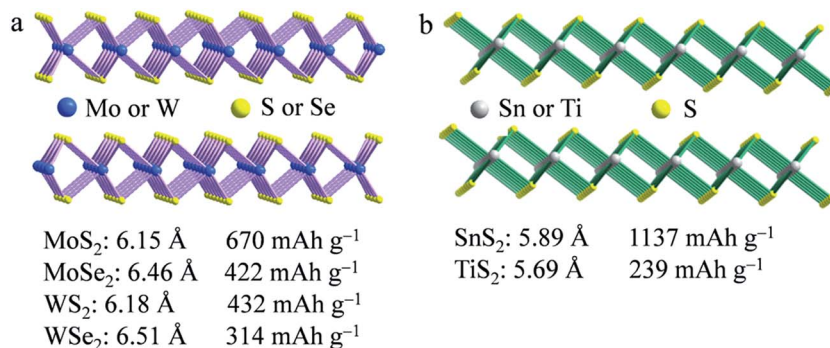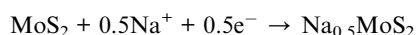
Fig. 1 Structure of the typical layered MX_2: (a) 2H-MoS_2, $MoSe_2$, WS_2 or WSe_2, and (b) SnS_2 or TiS_2. The interlayer spacings and the theoretical capacities of the typical MX_2 are given under their crystal structures.

batteries, photovoltaics, catalysis, and sensing. Among them, MoS_2 is an attractive host for ion intercalation because of its rich intercalation chemistry and structural peculiarities. The application of MoS_2 as a cathode for LIBs was patented and commercialized by Moli Energy as early as 1980.[26] However, it is becoming a hot subject to employ MoS_2 as a promising anode material in batteries. In particular, MoS_2 nanosheets, hierarchical structures, and related nanocomposites have recently been used as a variety of high-performance anodes. Nanostructuring, crystallographic modulation, conductive carbon modification and doping/alloying have been revealed to be effective approaches to enhance the electrochemical performance of MoS_2 electrodes. Until now, various MoS_2 nanostructured materials with different geometric shapes and morphologies have been intensively explored to obtain impressive electrochemical performance as SIB anodes.
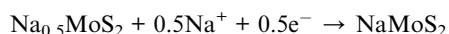
2.1.1 Sodium storage mechanism of MoS_2. In general, the Na-storage mechanisms for anodes can be classified into three types: insertion reaction, alloying–dealloying, and conversion reaction.[49–66,83,84] The Li-cycling mechanism of the MoS_2 anode has so far not been well understood, especially below the potential of 1.1 V vs. Li/Li^+. Similarly, the sodium storage mechanism in MoS_2 is ambiguous and generally regarded as two steps: intercalation and conversion. Wang et al. described the sodiation–desodiation process in detail based on the XRD analysis as follows:[85]
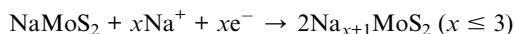
1st discharge process.
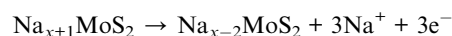1st plateau: intercalation reaction

$$MoS_2 + 0.5Na^+ + 0.5e^- \rightarrow Na_{0.5}MoS_2$$

2nd plateau: intercalation reaction

$$Na_{0.5}MoS_2 + 0.5Na^+ + 0.5e^- \rightarrow NaMoS_2$$

3rd plateau: conversion reaction

$$NaMoS_2 + xNa^+ + xe^- \rightarrow 2Na_{x+1}MoS_2 \ (x \leq 3)$$

1st charge process: conversion reaction

$$Na_{x+1}MoS_2 \rightarrow Na_{x-2}MoS_2 + 3Na^+ + 3e^-$$

Subsequent cycles: conversion reaction

$$Na_{x-2}MoS_2 + yNa \leftrightarrow Na_{x+y-2}MoS_2 \ (y \leq 3)$$
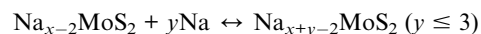
As for the sodium-ion pseudocapacitors, the reaction can be represented as:

$$Na_nMoS_2 \ (n \leq 3) \leftrightarrow Na_{n-m}MoS_2 + mNa^+ + me^- \ (m < n)$$

Park et al. demonstrated the Na^+ ion storage possibility using commercial MoS_2 and a capacity of 85 mA h g^{-1} at 0.4–2.6 V over 100 cycles based on an intercalation–deintercalation reaction.[86] Recently, ab initio calculations on Na-intercalation in all structural polytypes of MoS_2 were conducted by Medhekar et al.[87] They found that Na^+ ions generally occupy octahedral or distorted octahedral sites within the interlayer van der Waals spaces upon intercalation. Na^+ ion intercalation causes a phase transformation from the 2H to 1T phase, while it is thermodynamically stable across the entire concentration range against the phase separation of Na. The calculated energy barrier was 0.68 and 0.28 eV for Na-ion diffusion in 2H- and 1T-MoS_2, indicating moderately fast charge–discharge rates, respectively. These results suggest that the 1T polytype obtained via exfoliation of the 2H polytype shows better electrochemical performance arising from its inherent metallic electronic structure, higher capacity for Na^+ ions and their fast motilities. More importantly, Wang and coworkers investigated a series of two-phase structural transitions of MoS_2 during the intercalation at the atomic scale by aberration-corrected scanning transmission electron microscopy (STEM).[88] They found that MoS_2 experienced a series of two-phase transitions upon Na insertion, the phases including 2H-MoS_2, 2H-$Na_{0.5}MoS_2$, 1T-$Na_{0.5}MoS_2$, 1T-$NaMoS_2$ and Na_xS, as shown in Fig. 2. Upon discharge, Na^+ ion first intercalated to every other interlayer of few-layered 2H-MoS_2 (Fig. 2b, f and j), and then intercalated

Table 1 Recent advances in sodium storage performance for layered MX$_2$-based materials

Materials	Morphologies	Cycling performance		Rate performance		
		Capacity (mA h g^{-1})/cycles	Current (A g^{-1})	Capacity (mA h g^{-1})	Current (A g^{-1})	Ref.
MoS$_2$	Ultrathin nanosheets	251/100	0.32	300	0.32	92
MoS$_2$	Worm-like structure	410/70	0.0617			94
MoS$_2$/C	Microspheres	390/2500	1	244	20	117
MoS$_2$/C	Nanosheets	400/300	0.67	390	1.34	112
MoS$_2$@C	Nanotubes	512/200	0.2	370	5	114
MoS$_2$/C	Nanosheets	286/100	0.08	205	1	119
MoS$_2$–C	Nanotubes	415/200	1	187	20	95
MoS$_2$–C	Nanosheets	390/100	0.1	290	2	111
MoS$_2$@ACNTs	Tubes	461/150	0.5	396	1.6	113
MoS$_2$@ACNTs	Nanofiber	253/100	10	75	50	98
MoS$_2$/CNTs	Nanosheets	459/80	0.2	328	0.5	56
MoS$_2$/graphene	Microspheres	323/600	1.5	234	10	121
MoS$_2$/graphene	Nanosheets	312/200	0.1	247	2	85
MoS$_2$/graphene	Flaky structure	227/300	0.32	352	0.64	123
MoS$_2$/graphene	Paper	218/20	0.025	173	0.2	124
MoS$_2$/graphene	Nanoparticles	305/50	0.1	214	1	125
Expanded MoS$_2$–graphene	Nanoflowers	195/1500	10	175	10	96
MoS$_2$–EDA	Tubes	565/15				106
MoS$_2$–PEO	Particles	119/70	0.05	112	1	107
MoS$_2$/HfO$_2$	Nanosheets	636/100	0.1	347	1	128
MoS$_2$/Ni$_3$S$_2$@MoS$_2$	Network	200/400	2	283	5	126
Mo(Se$_{0.85}$S$_{0.15}$)$_2$:C	Nanotubes	312/100	1	360	2	109
MoSe$_2$	Nanospheres	345/200	0.0422	212	4.223	134
MoSe$_2$	Yolk–shell microspheres	433/50	0.2	345	1.5	137
MoSe$_2$	Nanoplates	369/50	0.0422	250	4.222	133
MoSe$_2$/CNTs	Fullerene-like structure	296/250	1	255	5	138
C–MoSe$_2$/rGO	Nanosheets	445/350	0.2	228	4	140
MoSe$_2$@PHCS	Hollow spheres	580/100	0.2	400	1.5	135
MoSe$_2$@MWCNTs	Nanosheets	459/90	0.2	385	2	139
MoSe$_2$/CF	Nanosheets	387/100	0.2	163	5	141
WS$_2$	Nanowires	330/1400	1	236	5	145
WS$_2$/C	Porous structure	219/300	0.5	81	5	148
WS$_2$-3D RGO	Microspheres	334/200	0.2	287	0.9	147
WS$_2$@graphene	Nanosheets	94/500	0.64	∼150	1.28	146
WSe$_2$/C	Nanoplates	270/50	0.2	208	1	151
SnS$_2$	Nanosheets	647/50	0.1	435	2	169
SnS$_2$ NC/EDA–RGO	Sheets	480/1000	1	250	11.2	175
SnS$_2$/rGO	Nanosheets	286/1000	0.8	337	12.8	161
SnS$_2$/graphene	Flakes	610/300	0.2	326	4	164
SnS$_2$–graphene	Sheets	500/400	1	544	2	160
SnS$_2$–NGS	Nanosheets	450/100	0.2	148	10	174
SnS$_2$@graphene	Nanoplatelets	670/60	0.02	463	0.685	162
GO–SnS$_2$	Nanosheets	450/100	0.5	340	2	178
SnS$_2$/C	Nanospheres	570/100	0.05	360	1	176
SnS–MoS$_2$	Yolk–shell structure	396/100	0.5	238	7	127
TiS$_2$	Nanoplatelets	142/300	0.48	101	2.4	186

into the empty layers (Fig. 2c, g and k) before the former interlayers were fully occupied. Meanwhile, the sulfur planes glide along an interlayer atomic plane to produce 1T-MoS$_2$. Finally, Na$^+$ ions filled all the interlayers (Fig. 2d, h and i) of MoS$_2$ (Fig. 2a, e and i). It was also shown that when more than 1.5 Na$^+$ ions per formula of MoS$_2$ were intercalated, Na$_x$MoS$_2$ would decompose to Na$_x$S and Mo, and the structural transformation would be irreversible. Gao et al. further proved the two-phase reaction and found that the two-phase reaction for the Na$^+$ ion insertion into MoS$_2$ nanosheets was initiated by nucleation of a new phase of NaMoS$_2$ followed by propagation of the phase boundary using in situ high-resolution TEM.[89] Furthermore, a planar microscale battery was designed to study the topographical changes of MoS$_2$ during the discharge–charge cycles.[90] Atomic force microscopy (AFM) revealed that the permanent structural wrinkling of sodiated MoS$_2$ was observed at 0.4 V, while the SEI layer on the MoS$_2$ electrode formed around 1.5 V before sodium intercalation. Besides Na$^+$ ion intercalation, MoS$_2$ has been proven to be converted into Mo and Na$_2$S with additional substantial gain in capacity (∼3 Na$^+$ ion reaction, ∼501 mA h g^{-1}) when further deeply discharged to a lower voltage (0.01 V).[85] The discharge product,

7670 | J. Mater. Chem. A, 2017, 5, 7667–7690

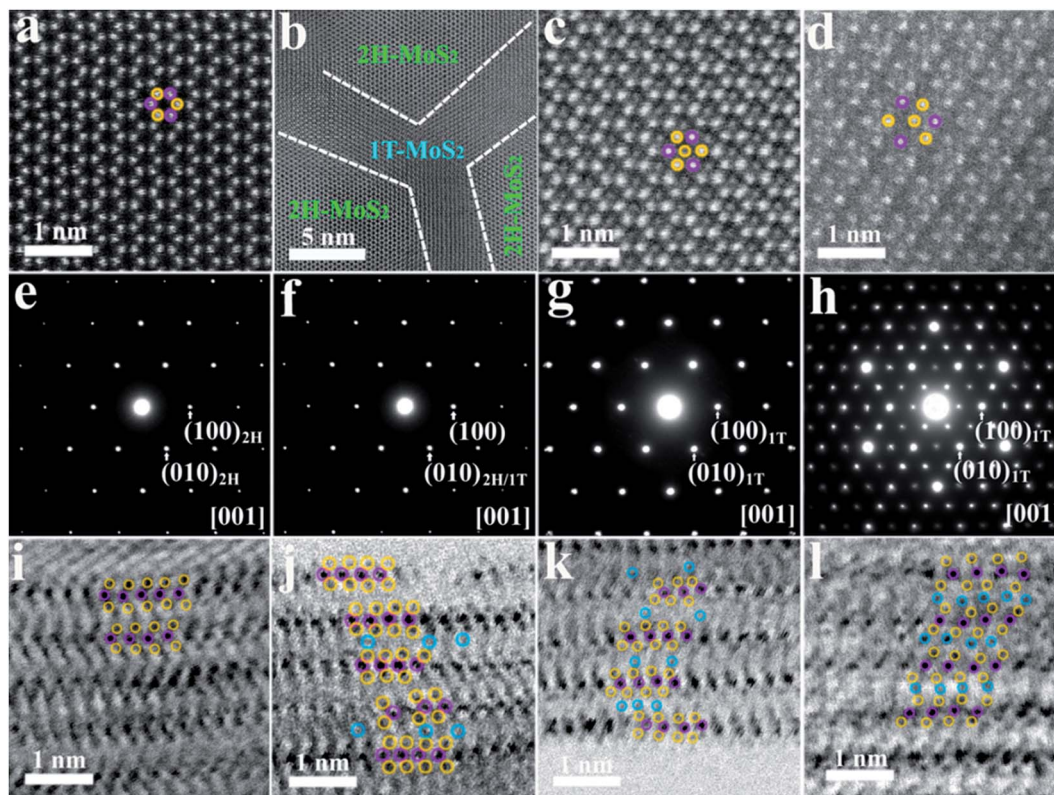This journal is © The Royal Society of Chemistry 2017

Fig. 2 High-angle annular dark-field (HAADF), and selected area electron diffraction (SAED) images of commercial MoS$_2$ in Cell-60 (a and e), Cell-80 (b and f), Cell-160 (c and g), and Cell-256 (d and h) along the [001] zone axis and the annular bright field (ABF) images of the as prepared nano-MoS$_2$ (i) with cutoff at 1.0 V (j), 0.8 V (k), and 0.2 V (l) along the [100] zone axis. The purple, yellow, and blue circles are overlaid in the image for Mo, S, and Na atoms, respectively. Reprinted with permission from ref. 88. Copyright 2014 American Chemical Society.

Na$_2$S, could afford better conductivity than Na$_2$O as typically formed from a deep conversion reaction of metal-oxide compounds .[91]

2.1.2 Nanostructure engineering of MoS$_2$ nanostructures

Several synthesis approaches have been reported to prepare well-constructed MoS$_2$ nanostructure anodes including nano-particles, nanosheets, nanoflowers, nanotubes, nanoplates, self-assembling hierarchical architectures and thin films as shown in Fig. 3.[92–98] Nanostructuring of MoS$_2$ can enhance the electrochemical performance compared with bulk materials. In particular, fabrication of hierarchical nanostructures attracts much interest because of the extraordinarily high active surface/interface and robust stability. Electrode materials with hierar-chical architectures exhibit intriguing properties by taking advantages of both the nanometer-size effects and the high stability of the secondary-structure assemblies. On the other hand, it is believed that the expanded and gradually exfoliated interlayers can decrease the barriers for Na$^+$ ion insertion and extraction, thus reducing the charge transfer resistance and offering more active sites for Na$^+$ ion storage.

MoS$_2$ micro-particles constructed from small nanosheets were synthesized by a solid-state reaction at 700 °C and used as the anode material for SIBs.[93] When the binder was optimized as sodium alginate, it could only deliver a reversible capacity of

420 and 290 mA h g^{-1} at currents of 50 and 150 mA g^{-1}, respectively, indicating a passable capacity and rate perfor-mance. Exfoliating bulk MoS$_2$ into few-layer sheets or individual monolayers can allow for an enhanced adsorption of Na$^+$ ions on both sides and faster diffusion rates. Through liquid-phase exfoliation, bulk MoS$_2$ powder was converted into mono-layers.[99] The exfoliated MoS$_2$ nanosheets showed sodiation and desodiation capacities of 254 and 164 mA h g^{-1} in the first cycle, respectively. The discharge capacities decreased gradually to 161 mA h g^{-1} at the 50th cycle with a coulombic efficiency (CE) of 97%. This exfoliated MoS$_2$ electrode showed stable cycling behavior up to 100 cycles. In fact, the observed initial sodiation capacity is higher than that of a previous report based on pris-tine bulk MoS$_2$.[86] Su et al. successfully prepared few-layer MoS$_2$ nanosheets with the thickness of ∼10 nm through ultrasonic exfoliation of bulk MoS$_2$ powder in formamide solution.[92] This unique architecture is in favor of the high-rate transportation of Na$^+$ ions due to the short diffusion paths provided by the ultrathin thickness and the large interlayer spacing (6.38 Å). MoS$_2$ nanosheets delivered high initial discharge capacity (above 800 mA h g^{-1}), and presented high capacity retention. After 100 cycles, this MoS$_2$ electrode maintained 330, 305 and 251 mA h g^{-1} at currents of 80, 160, and 320 mA g^{-1}, respec-tively, which is much better than that of bulk MoS$_2$. This result confirms that the exfoliated MoS$_2$ nanosheets can tolerate high
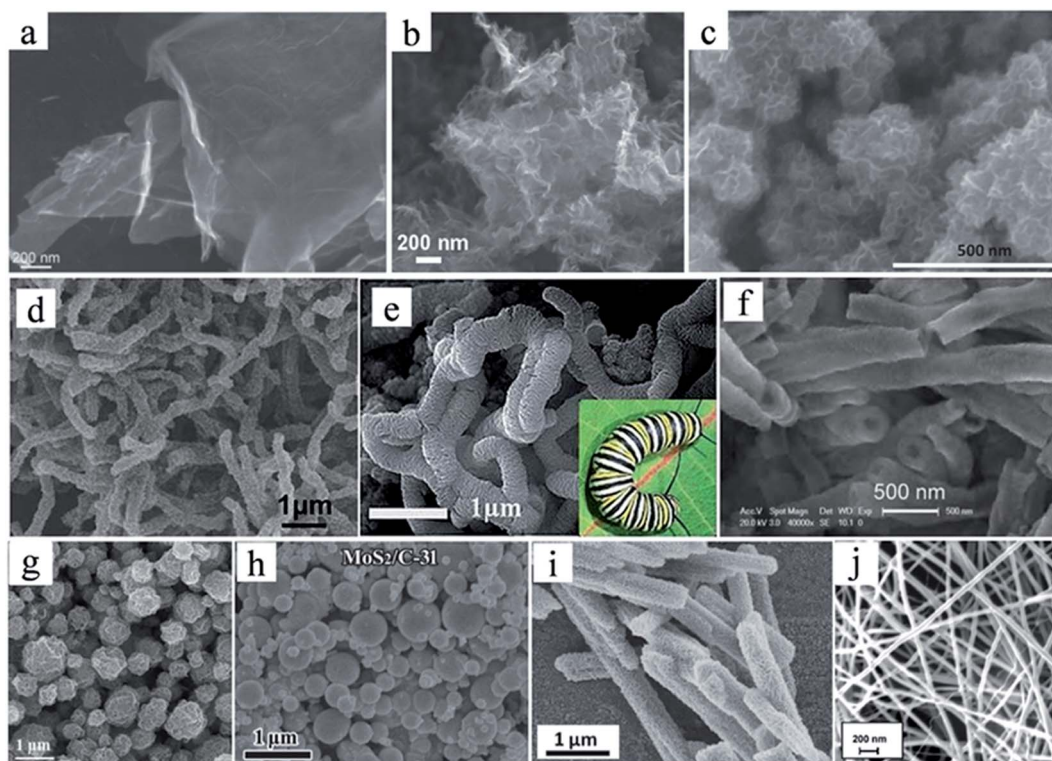
Fig. 3 SEM images of MoS$_2$ nanostructures used as anode materials in SIBs. (a) Reprinted with permission from ref. 92, Copyright (2015) by Wiley-VCH; (b) reprinted with permission from ref. 123, Copyright (2015) by Wiley-VCH; (c) reprinted with permission from ref. 112, Copyright (2015) by Wiley-VCH; (d) reprinted with permission from ref. 113, Copyright (2016) by The Royal Society of Chemistry; (e) reprinted with permission from ref. 94, Copyright (2015) by The Royal Society of Chemistry; (f) reprinted with permission from ref. 95, Copyright (2016) by Elsevier; (g) reprinted with permission from ref. 121, Copyright (2015) by Wiley-VCH; (h) reprinted with permission from ref. 117, Copyright (2016) by Wiley-VCH; (i) reprinted with permission from ref. 114, Copyright (2016) by Wiley-VCH; (j) reprinted with permission from ref. 98, Copyright (2014) by Wiley-VCH.

current charge/discharge cycling owing to the small size, the large exposed surface, and the metallic phase of exfoliated MoS$_2$ nanosheets.

Exfoliated MoS$_2$ nanosheets with mono- or few-layers always suffer from poor cycling stability. To improve the cycling performance, hierarchical architectures constructed from MoS$_2$ nanosheets were designed and also employed as anode materials for SIBs. Xu et al. successfully prepared ultralong worm-like MoS$_2$ nanostructures using a solvent-mediated solvothermal process.[94] When evaluated as SIB anode materials, they delivered a sodium insertion capacity of about 675.3 mA h g^{-1} in the voltage range of 3.0–0.01 V in the first cycle. The irreversible capacity in the first cycle is as high as 181.1 mA h g^{-1}, which may be caused by the decomposition of the electrolyte for formation of SEI film and trapping in the nanoclusters or defect sites of a fraction of Na$^+$ ions. After stable SEI film formation, the discharge capacity shows a stable value of 410.5 mA h g^{-1} within 80 cycles, showing a capacity retention of 83.1% compared with that in the second cycle. The average fade of the subsequent specific capacity is just 0.21% in each cycle. Other hierarchical structures such as hollow spheres, micro-boxes and nanotubes have been explored as LIB anodes and exhibited impressive performance.[100–104] Considering the similar electrochemical behavior between SIBs and LIBs, these hierarchical nanoarchitectures should be attempted to be used as electrode materials in SIBs in the near future.

2.1.3 Interlayer expansion of MoS$_2$ nanosheets. The interlayer between two adjacent MoS$_2$ monolayers plays an important role in sodium ion intercalation and extraction. MoS$_2$ has a (002) interlayer spacing of 0.615 nm. Expanded interlayers can work as efficient ion migration channels, which is helpful to improve charge/discharge kinetics. Interlayer-expanded MoS$_2$ nanosheets with a decoupling state are expected. Much work has also been done to study the effect of the expanded interlayer intercalated with guest molecules (carbon, graphene, organic small molecules or polymers) on the anode electrochemical performance in SIBs. Both the ion intercalation energy and the ion diffusion energy barrier of interlayer-expanded 2H-MoS$_2$ are lowered based on the density functional theory (DFT) simulations.[105] Wang et al. obtained nano-MoS$_2$ with expansion of their cells along the c axis through intercalating guest species, including amorphous carbon, polyvinyl pyrrolidone (PVP), ethylene diaminetrimolybdate (EDA) derived small molecules into the nano-scaled MoS$_2$.[106] The c value of the nano-MoS$_2$ is calculated to be 6.63, 7.05, 10.02, and 11.59 Å for GMS, MoS$_2$–PVP, MoS$_2$–EDA, and GMS–C, respectively. GMS–C and MoS$_2$–PVP exhibit superior cycling stability, and their capacities increase with cycling. In terms of capacity and cycling stability,

7672 | J. Mater. Chem. A, 2017, 5, 7667–7690

This journal is © The Royal Society of Chemistry 2017

MoS_2–EDA shows the best electrochemical performance. A high reversible Na-storage capacity of 565 mA h g^{-1} is obtained for MoS_2–EDA, attributed to C–S and O–S bonding enhancing the structural stability of the nano-MoS_2. In addition, Li *et al.* designed interlayer-expanded materials as general large Na$^+$ ion hosts to tackle the kinetic challenges. Poly(ethyleneoxide)-intercalated MoS_2 composites (PEO–MoS_2) with tunable interlayer spacings were prepared *via* a facile exfoliation-restacking method as highlighted in Fig. 4.[107] The interlayer spacing of MoS_2 was increased from 0.615 nm to 1.45 nm by insertion of controlled amounts of PEO. The PEO$_{2L}$–MoS_2 with two layers of PEO between two slabs of MoS_2 possessed the largest interlayer spacing of 1.4 nm, showing the highest and stable capacity (225 mA h g^{-1}) within 70 cycles among the samples with different interlayer spacings. The increased interlayer spacing leads to an enhanced Na-ion diffusivity, which is responsible for the improvement in electrode performance. This strategy may be extended to a wide range of layered MX_2 electrode materials for large Na$^+$ ion intercalation.

2.1.4 Doping or alloying of MoS_2 nanostructures

MoS_2 with high conductivity is necessary for developing the sodium storage performance. Doping or alloying was employed to improve the electrical conductivity of MoS_2. Fullerene-like Re-doped MoS_2 nanoparticles exhibited enhanced cyclability compared with bare MoS_2.[108] It is because electrical conductivity was enhanced and the number of diffusion channels (defects) along the *c* axis was increased after Re-doping. $MoSe_2$ has better conductivity than MoS_2 due to the smaller bandgap. Se has a large atom radius than S. Incorporation of Se into MoS_2 to form alloyed $MoS_{2x}Se_{2-2x}$ is beneficial to increase both the conductivity and the interlayer-spacing of MoS_2. In our group, we prepared MoS_2:C nanotubes by a solvothermal reaction, in which *in situ* carbon doping was achieved by carbonization of the octylamine molecules. $Mo(Se_{0.85}S_{0.15})_2$:C hierarchical nanotubes were obtained by selenizing the precursor of MoS_2 nanotubes at 900 °C.[109] As an anode material in SIBs, $Mo(Se_{0.85}S_{0.15})_2$:C hierarchical nanotubes exhibited good cycling stability and high rate capability. They gave an initial discharge capacity of 524 mA h g^{-1} with a CE of 82.3% at a current density of 200 mA g^{-1} and the discharge capacity was maintained at 421 mA h g^{-1} after 100 cycles, close to the theoretical specific capacity of 422 mA h g^{-1}. After increasing the current densities to 500 and 1000 mA g^{-1}, the nanotubes showed reversible capacities of 379 and 312 mA h g^{-1} after 100 cycles, with capacity retentions of 101.9% and 97.8%, demonstrating outstanding cycling stability and fast reaction kinetics. The hollow interior, hierarchical organization, layered structure, and carbon doping were beneficial for fast Na$^+$ ion and
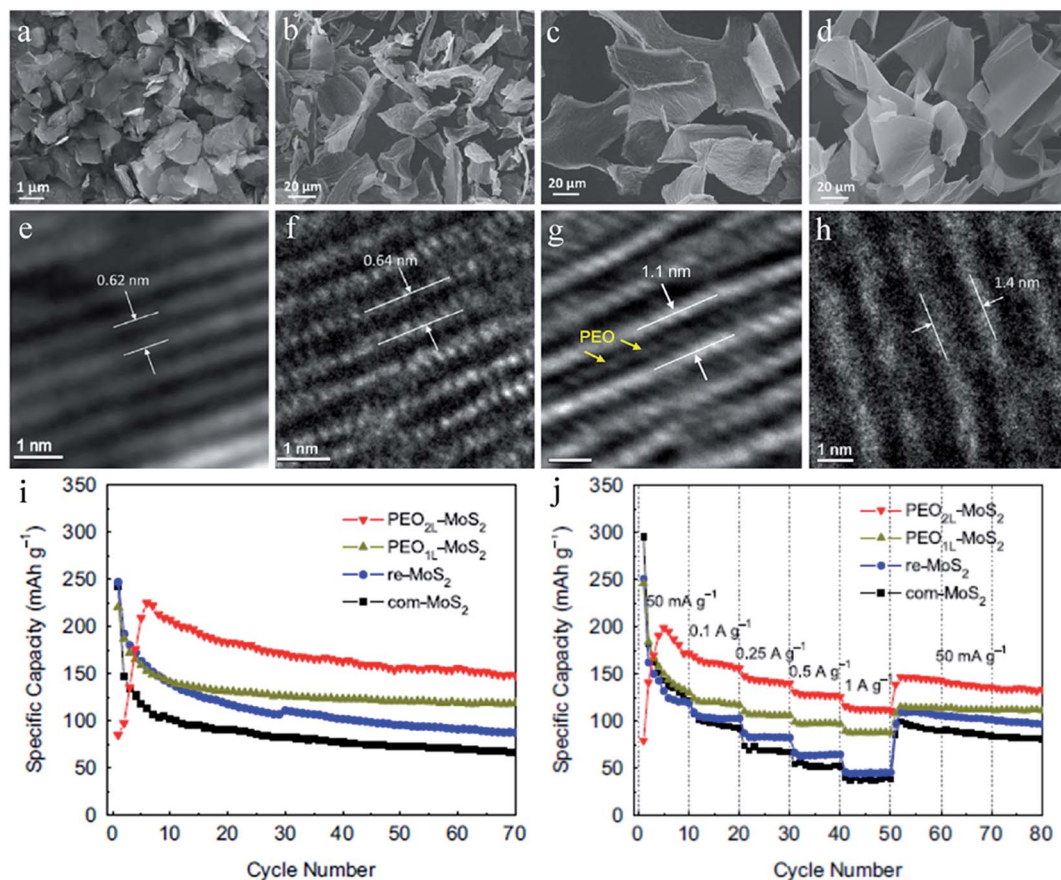

Fig. 4 (a–d) SEM images of the morphology, (e–h) HRTEM images, (i) cycling performance and (j) rate capability of com-MoS_2, re-MoS_2, PEO$_{1L}$–MoS_2 and PEO$_{2L}$–MoS_2. Reprinted with permission from ref. 107, Copyright (2016) by Elsevier.

electron kinetics, leading to stable cycling performance and high rate capabilities. In addition, we have prepared 2H-$MoS_{2x}Se_{2-2x}$ ($x = 0.22$) mesoporous nanospheres assembled from several-layered nanosheets by sulfurizing freshly prepared 1T-$MoSe_2$ nanospheres and served as a robust host material for sodium storage.[110] This nanosphere anode can maintain a stable capacity of 407 mA h g^{-1} after 100 cycles without fading at a high current density of 2.0 A g^{-1}. The superior electrochemical performance of the 2H-$MoS_{2x}Se_{2-2x}$ electrode suggests a promising way to design advanced sodium host materials through an alloying process.

2.1.5 Carbon materials modified MoS$_2$ electrodes

Owing to the poor conductivity and serious polarization, MoS_2 electrodes suffer from cracking and crumbling during repeated charge–discharge process owing to the reaction with Na at a low voltage range, which leads to significant capacity fading by loss of inter-particle contact in the electrode. These problems could not be easily solved only by the preparation of nanostructures. Fabrication of MoS_2 composite-type materials with an effective matrix for volume variations has been considered as a promising alternative. The combination of a nanostructure and carbon matrix can affect each other, offering an effective scenario for the target materials with state of the art properties. In fact, nanostructured composites are generally reliable to alleviate volume change problems and enable MoS_2 with superior rate capability and good durability. Recently, enormous efforts have been devoted to construct MoS_2 composites as anode materials for SIBs.

Amorphous carbon is a widely used additive to enhance the conductivity of the electrode materials for energy storage. An exfoliated MoS_2–C composite was also prepared *via* simple chemical exfoliation and a hydrothermal method by Dou's group.[111] As an anode material for SIBs, the obtained MoS_2–C showed a high capacity of ~400 mA h g^{-1} at 100 mA g^{-1} after 100 cycles. Outstanding rate capability was also achieved with a capacity of 290 mA h g^{-1} at 5C. Wang's group reported the synthesis of MoS_2/C nanospheres by a one-step hydrothermal reaction.[112] The MoS_2/C nanospheres delivered a reversible capacity of 520 mA h g^{-1} at 0.1C and maintained at 400 mA h g^{-1} for 300 cycles at a high current density of 1C, demonstrating its exceptional cycling ability and fast reaction kinetics. Such an excellent electrochemical performance was ascribed to the carbon coating, small size and the formation of a stable SEI layer. Xu *et al.* built a novel one dimensional architecture by MoS_2 nanosheets and amorphous carbon nanotubes (MoS_2@-ACNTs) through a step-wise route.[113] The MoS_2@ACNT electrode exhibited a high discharge capacity of 461 mA h g^{-1} even over 150 cycles at 500 mA g^{-1}. The improved electrochemical performance can be ascribed to the synergistic effect between MoS_2 and ACNTs and smart architecture of the electrode material. MoS_2 nanotubes and amorphous carbon were generated synchronically to form a MoS_2@C nanotube composite based on the Kirkendall effect by a facile hydrothermal process.[114] For Na$^+$ ion storage, at 0.5C the MoS_2@C composite showed an initial discharge capacity of 640 mA h g^{-1} and

demonstrated a capacity retention of 80% after 200 cycles. The remarkable electrochemical performances should be attributed to the synchronically formed carbon and the structural superiority of the MoS_2@C nanotubes, which not only improved the electronic conductivity, but also alleviated the huge inherent volume changes. MoS_2/C nanosheets were synthesized using ion exchange resins as the carbon source.[115] This composite can deliver good electrochemical performance due to the synergistic effect between the uniformly distributed, ultrathin MoS_2 nanosheets and the carbon. Multiwalled carbon@MoS_2@-carbon with a 3D nanoweb-like structure was designed and constructed.[116] This novel structure can exhibit outstanding reversible capacity (1045 mA h g^{-1}), good rate behavior (817 mA h g^{-1} at 7000 mA g^{-1}), and cycling performance (747 mA h g^{-1} after 200 cycles at 700 mA g^{-1}) as the SIB anode material. The sandwiched MoS_2 nanosheets between two layers of porous carbon can be protected from aggregation, leading to outstanding electrochemical performance.

Electrospinning process is a popular method to fabricate MoS_2/C composites.[98,117,118] Single-layered ultrasmall nanoplates of MoS_2 embedded in thin carbon nanowires were successfully prepared by electrospinning.[98] For sodium storage, a specific capacity of 854 mA h g^{-1} was achieved at 0.1 A g^{-1}, and capacities of 484 and 253 mA h g^{-1} can be obtained at 1 and 10 A g^{-1} after 100 cycles, respectively. The outstanding rate performance and cycling stability of this single layered MoS_2/carbon nanowire composite can be ascribed to the unique nanostructure: (1) the single-layered nature supported by spatial isolation in the carbon matrix minimized transport problems. (2) The carbon matrix, as a good mixed conductor, enabled the nanoplates to be electrochemically perfectly coupled. Chen's group reported a one-step spraying synthesis of MoS_2/C microspheres and their enhanced sodium storage capability as shown in Fig. 5.[117] The as-synthesized mesoporous MoS_2/C microspheres with 31 wt% carbon have been applied as an anode material for SIBs, demonstrating long cycling stability (390 mA h g^{-1} after 2500 cycles at 1.0 A g^{-1}) and high rate capability (312 mA h g^{-1} at 10.0 A g^{-1} and 244 mA h g^{-1} at 20.0 A g^{-1}). The superior electrochemical performance can be ascribed to the uniform distribution of ultrathin MoS_2 nanosheets in mesoporous carbon frameworks. This kind of a structure can effectively improve the electronic and ionic transport through MoS_2/C microspheres and minimize the influence of pulverization and aggregation of MoS_2 nanosheets in the cycling process.

When carbon was used as the substrate to support the MoS_2 growth, the electrochemical performance could also be enhanced remarkably.[119] MoS_2 nanosheets on carbon derived from a paper towel (MoS_2@C) were successfully prepared as a freestanding anode material for SIBs by a hydrothermal reaction. At a high current density of 1000 mA g^{-1}, it can show a high first EC and maintain a stable capacity of 286 mA h g^{-1} within 100 cycles. This impressive performance as an SIB anode can be ascribed to the hierarchical structure of the hybrid, which provided shortened ionic diffusion pathways and reduced the mass-transfer limitation. On the other hand, MoS_2 nanosheets are connected with conductive carbon fibers, thus
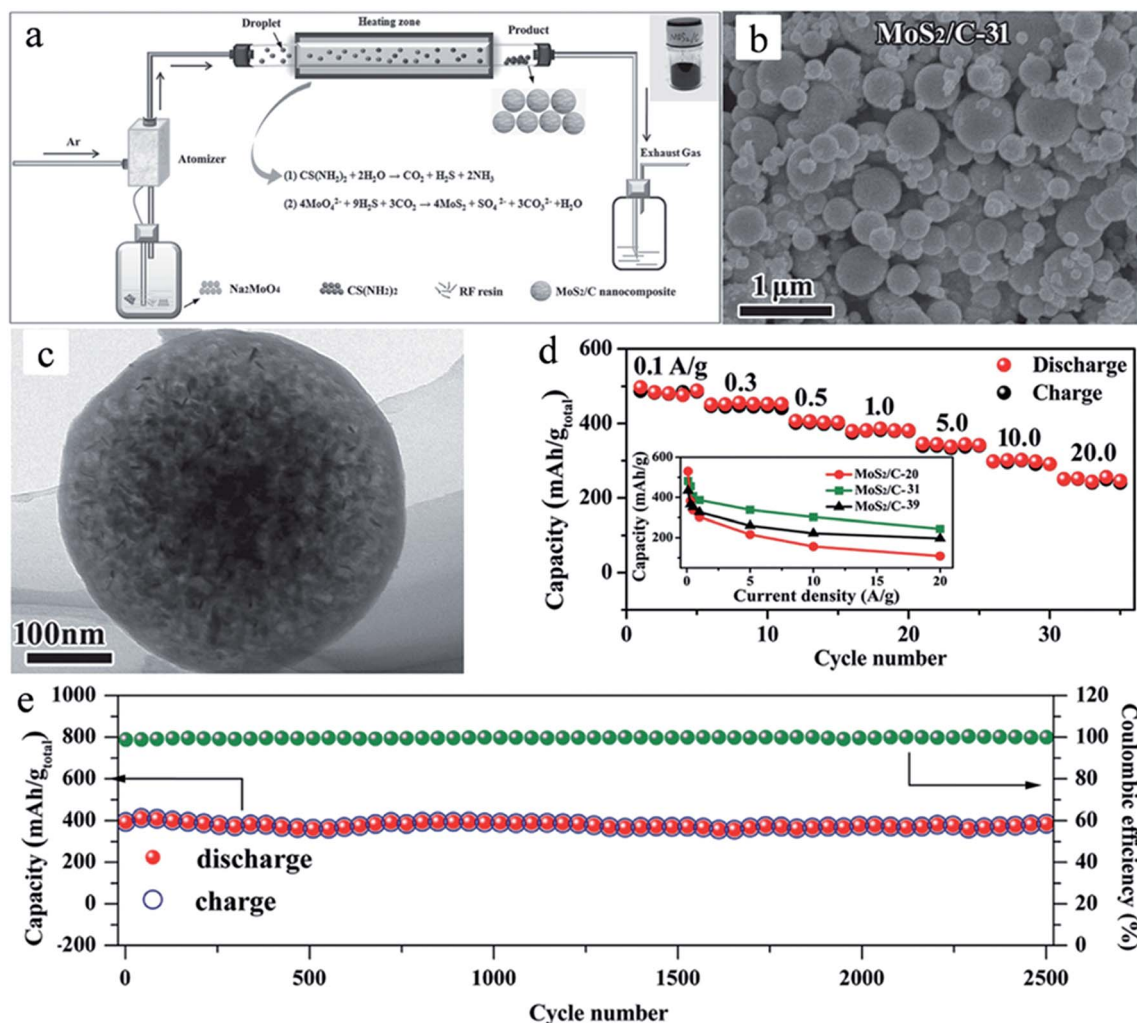
7674 | *J. Mater. Chem. A*, 2017, 5, 7667–7690

This journal is © The Royal Society of Chemistry 2017

Fig. 5 (a) Schematic of the spraying synthesis of mesoporous MoS_2/C microspheres. (b) SEM, (c) TEM, (d) rate capability and (e) cycling performance at 1000 long-term cycling performance and the corresponding CE at 1.0 A g^{-1} for MoS_2/C-31. Reprinted with permission from ref. 117, Copyright (2016) by Wiley-VCH.

affording good current collector/active material electrical contacts and low charge transfer resistance.

Carbon nanotubes (CNTs) have been proved to be viable anode materials due to their lightweight, robust mechanical and electrical properties, and ability to support high capacity materials. A flexible free-standing MoS_2/CNT membrane was prepared using vacuum filtration of high-quality MoS_2 nanosheet dispersion mixed with CNTs.[120] This membrane can be directly employed as the working electrode of SIBs. A striking specific capacity of >400 mA h g^{-1} and a volumetric capacity of ~650 mA h cm^{-3} could be achieved. These values are outstanding and even superior to those of most SIB electrode materials, as enabled by the hierarchical architecture prepared with the CNT network.

Graphene can play an important role in electrochemical energy storage applications, even when it takes no active part in the energy storage mechanism. Owing to its high electrical conductivity, it has been proposed as a conducting agent in SIB electrodes. In addition to the superior electrical conductivity, its

high thermal conductivity facilitates heat dissipation when a high current load is required. This might improve the intrinsic safety of the devices. Additionally, formation of graphene-based hybrids with other inorganic/organic compounds makes graphene a promising functional substrate for SIB electrodes. MoS_2/graphene composites always display impressive performance as SIB anode materials.[85,121–125] In Kang's group, novel 3D graphene microspheres divided into several tens of uniform nanospheres coated with few-layer MoS_2 layers were prepared through a one-pot spray pyrolysis process (Fig. 6).[121] The 3D MoS_2–graphene composite microspheres showed superior Na^+ ion storage capacities due to the synergistic effects of the reduced stacking of the MoS_2 layers and the 3D structure of the porous graphene microspheres. The capacity of the composite microspheres was 322 mA h g^{-1} at 1.5 A g^{-1} after 600 cycles with a high CE of 99.98%. Xie *et al.* also prepared a MoS_2/graphene composite with controllable heterointerfaces as the anode for SIBs by a facile hydrothermal method.[123] They revealed that the composite with more heterointerfacial areas had higher Na^+ ion
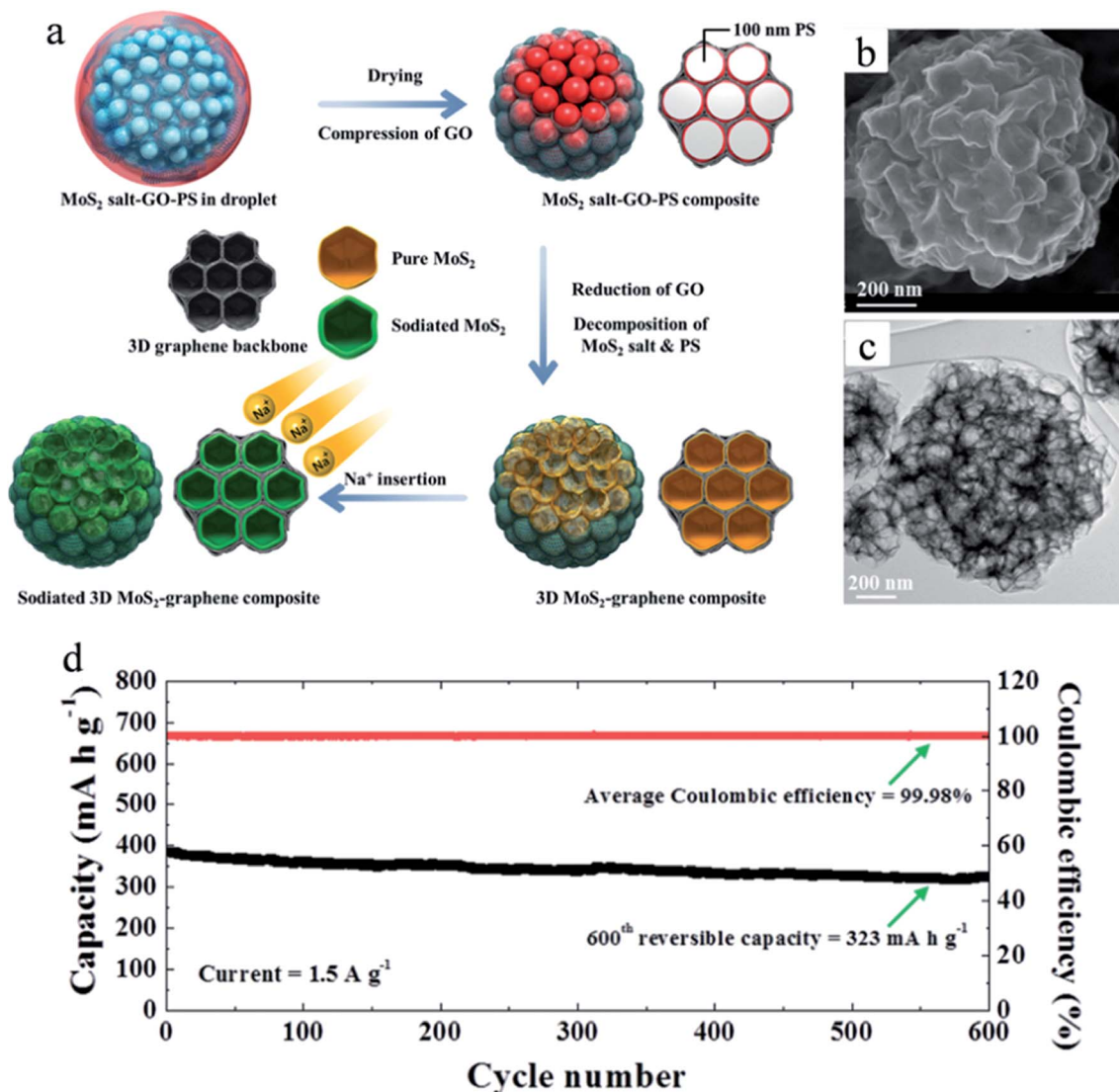
Fig. 6 (a) Schematic diagram for the formation mechanism of the 3D MoS$_2$–graphene composite microsphere by the one-pot spray pyrolysis and description of the Na$^+$ ion insertion process. (b) SEM, (c) TEM, (d) cycling performance of the 3D MoS$_2$–graphene composite microspheres. Reprinted with permission from ref. 121, Copyright (2015) by Wiley-VCH.

storage capacity, and the interfacial interaction also led to a significantly improved cycling performance. The composite with the largest heterointerfaces exhibited capacities of 254 and 227 mA h g^{-1} at 80 and 320 mA g^{-1} after 300 cycles, respectively. Layered freestanding papers can also be obtained through vacuum filtration of homogeneous dispersions consisting of acid-treated MoS$_2$ flakes in graphene oxide solution.[124] Mechanical tests involving static uniaxial tension revealed mechanical strength that was approximately 2–3 MPa and high failure strain (approximately 2%) in these materials. As an anode for SIBs, the first cycle charge capacity increased with increasing percentage of MoS$_2$ in the composite; 60MoS$_2$ (60 wt% MoS$_2$ in rGO/MoS$_2$ paper) showed the highest capacity of 338 mA h g^{-1}. After an initial drop in the capacities, the rGO/ MoS$_2$ composite electrode remained constant at 218 mA h g^{-1} for 60MoS$_2$, which was the best performing with 83% capacity

retention and approximately 98% average efficiency among three samples with different MoS$_2$ percentages.

The reported MoS$_2$–C composites usually have limited heterointerfaces. To increase the hetero-contact between MoS$_2$ and carbon for enhancing the conductivity of MoS$_2$, mono- or few-layered carbon (or graphene) is expected to sandwich with MoS$_2$ monolayers to form a MoS$_2$:C superstructure. In our group, we prepared novel hierarchical nanotubes assembled from 2D superstructure nanosheets consisting of alternative monolayers of MoS$_2$ and carbon which was transformed from the inserted octylamine as shown in Fig. 7.[95] As a result, the present MoS$_2$ hollow architecture shows a significantly expanded (002) interlayer spacing as large as 0.98 nm. Compared to the common MoS$_2$ and carbon composites, the 2D superstructure possesses an ideal interfacial contact between MoS$_2$ and carbon coupled with a substantially enlarged
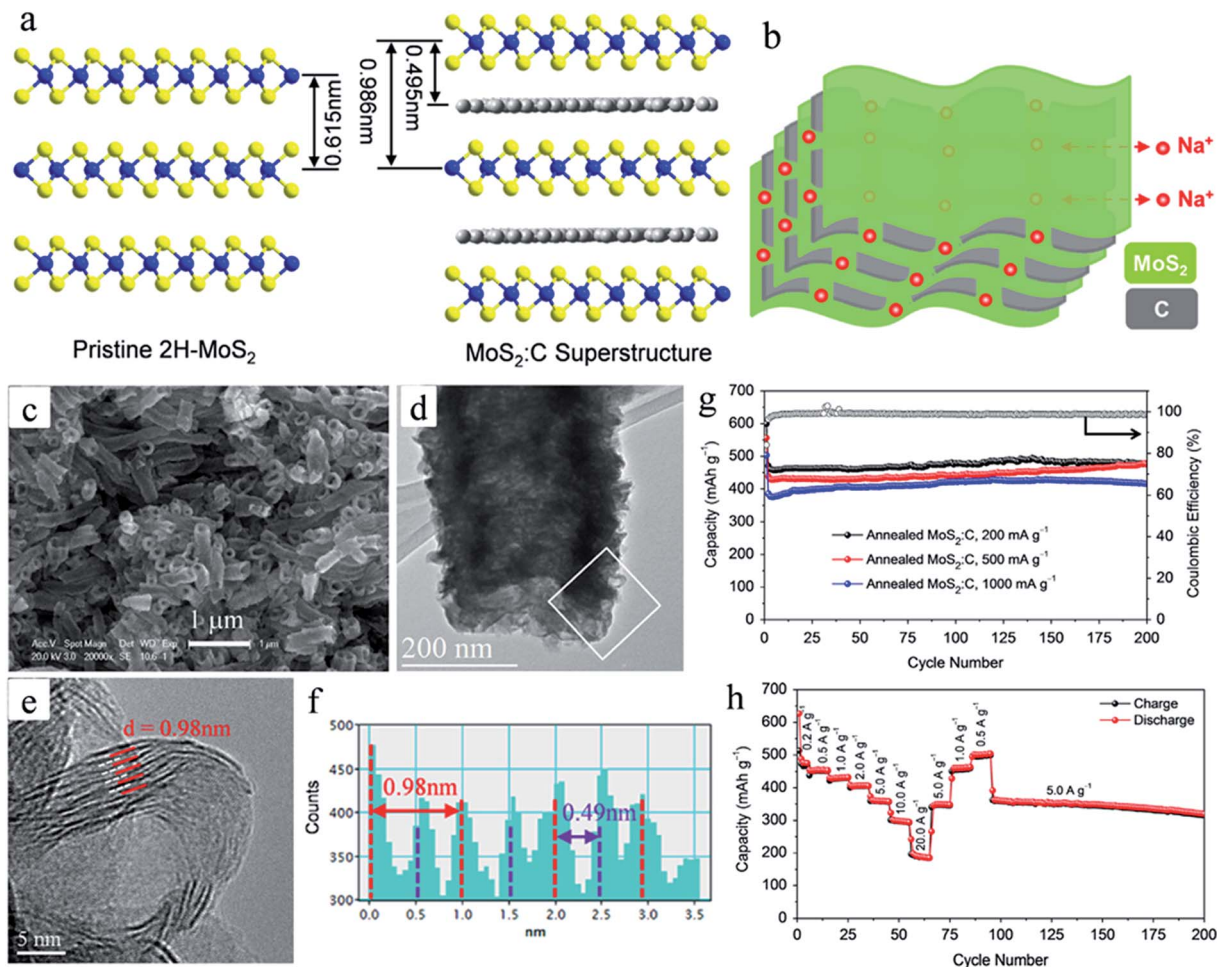
Fig. 7 (a) Structural models of the pristine 2H-MoS_2 and the MoS_2:C interoverlapped superstructure with expanded interlayer spacing; (b) schematic illustration of the rational design of the MoS_2:C interoverlapped superstructure with uncontinuous carbon monolayers benefiting Na^+ ion insertion/extraction; (c) SEM image, (d) TEM image, (e) HRTEM images of the MoS_2:C superstructure nanotubes after post thermal treatment. (f) Profile plot of the calibration for measuring the spacings in the panel. (g) Cycling performance and (h) rate performance of the annealed MoS_2:C nanotube electrode. Reprinted with permission from ref. 95, Copyright (2016) by Elsevier.

interlayer distance, allowing faster sodiation/desodiation kinetics. At the current density of 200 mA g^{-1}, the annealed MoS_2:C nanotube electrode delivers an initial discharge capacity of 620 mA h g^{-1} and charge capacity of 521 mA h g^{-1} with a first CE up to 84%. A capacity of 477 mA h g^{-1} can be obtained within 200 cycles with a high CE of 99%. Even after cycling at a high current of 1000 mA g^{-1}, a capacity of 415 mA h g^{-1} can be obtained after 200 cycles. A capacity as high as 187 mA h g^{-1} can be reached even after cycling at a current of 10 A g^{-1}, indicating excellent rate capability. The excellent rate and cycling performance of these superstructure nanotubes is attributed to the synergistic effects of MoS_2:C sandwiched superstructures with ideal atomic hetero-interfaces, 2D layered structures with an enlarged interlayer distance, three-dimensional (3D) hierarchical organization, and tubular hollow morphologies. It can be concluded that the enlarged interlayer can affect the structural stability and Na^+ ion motility in the sodiation/desodiation process. Hu *et al.* synthesized graphene-like MoS_2 nanoflowers with expanded interlayers of 0.67 nm by a hydrothermal method.[96] They could deliver

increased capacities in the initial 500 cycles and stable reversible discharge capacities of 300 mA h g^{-1} at 1 A g^{-1}, and 195 mA h g^{-1} at 10 A g^{-1} after 1500 cycles in the voltage range of 0.4–3.0 V. The increased capacities are derived from the gradually expanded and exfoliated interlayers, which actually provide more active Na^+ ion storage sites and lower energy barrier for Na^+ ion for intercalation/deintercalation.

2.1.6 MoS_2-based nanocomposites

Besides modification using carbon materials, sulfide and oxide materials are also used to construct composites with MoS_2 in order to enhance their sodium storage performance. MoS_2 nanocomposites including Ni_3S_2@MoS_2 coaxial nanofibers,[126] SnS–MoS_2 composite,[127] and HfO_2-coated MoS_2 nanosheets[128] have been studied as SIB anode materials. MoS_2/Ni_3S_2@MoS_2 hybrid nanofiber architectures were fabricated *via* a one-step PVP-assisted hydrothermal process.[126] In the hybrid architectures, elongated Ni_3S_2 nanofibers were wrapped with MoS_2 nanobelts to form core–shell Ni_3S_2–MoS_2 nanofibers with

This journal is © The Royal Society of Chemistry 2017

J. Mater. Chem. A, 2017, **5**, 7667–7690 | **7677**

a homogeneous heterointerface, which were further uniformly decorated with few-layer MoS_2 nanosheets (Fig. 8). The cycling performance of the $MoS_2/Ni_3S_2@MoS_2$ electrode was also outstanding even after 100 cycles. The stable capacities were about 483 mA h g^{-1} at a current of 200 mA g^{-1}, exhibiting 82.6% capacity retention. In contrast, the capacities of Ni_3S_2/MoS_2 and $Ni_3S_2@MoS_2$ electrodes continuously decayed under the same testing conditions. After 100 cycles, the Ni_3S_2/MoS_2 and $Ni_3S_2@MoS_2$ electrodes only delivered capacities of 277 and 199 mA h g^{-1}, with 60.7% and 50.4% capacity retention, respectively. The excellent electrochemical performance should be attributed to the high ion mobility as well as high electrochemical activity of the heterostructures based on the electrochemical impedance spectroscopy results. This clearly validated
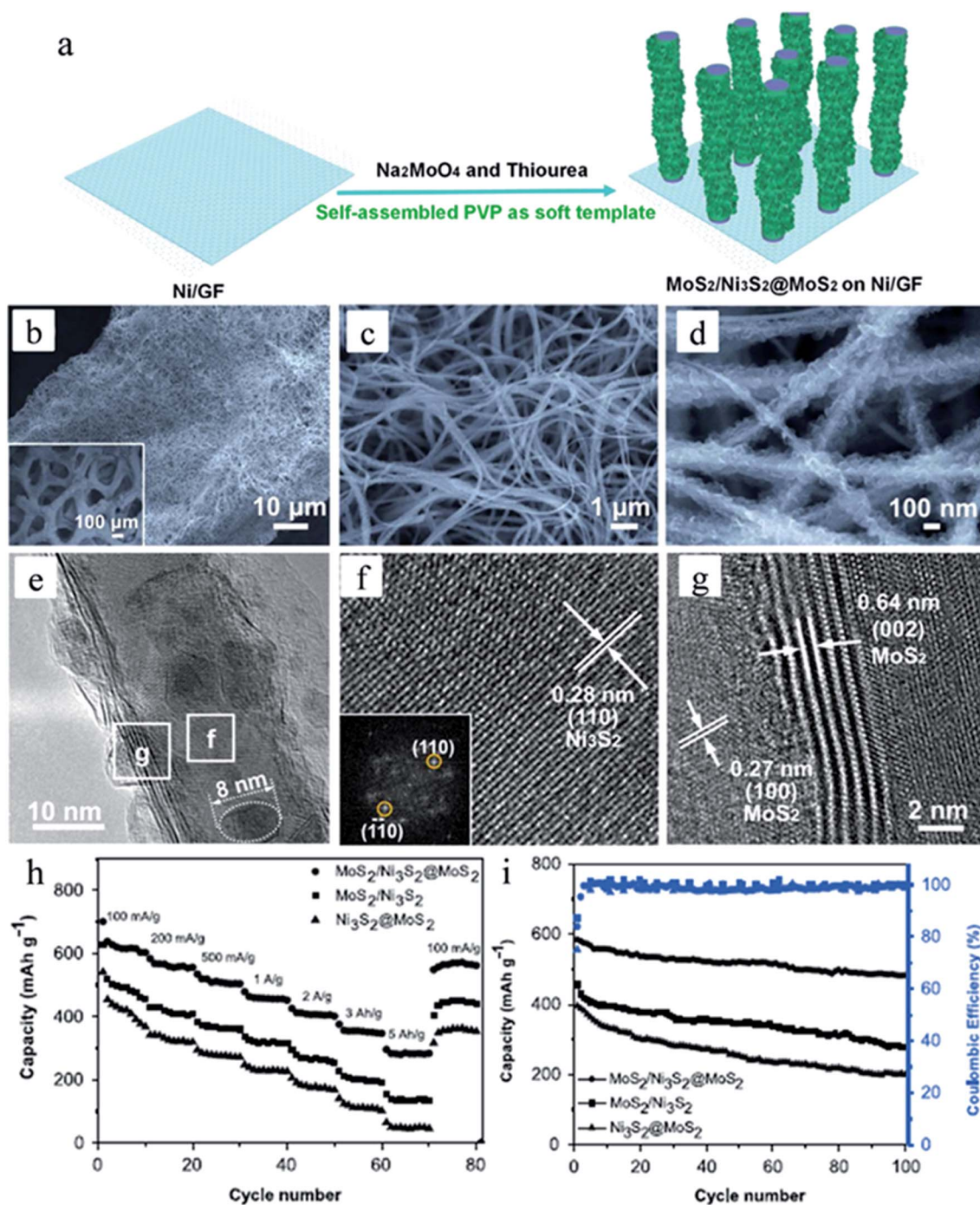

Fig. 8 (a) Schematic illustration of the synthesis process of the $MoS_2/Ni_3S_2@MoS_2$ heterostructure; (b)–(d) SEM images, (e) TEM images, (f) and (g) HRTEM images of the different areas of (e) (the inset of (f) shows the corresponding FFT pattern). (h) Capacity retention of three different electrodes at different current densities. (i) Cycling behaviors of the three different electrodes at a current density of 200 mA g^{-1}. Reprinted with permission from ref. 126, Copyright (2016) by Elsevier.

7678 | J. Mater. Chem. A, 2017, 5, 7667–7690

This journal is © The Royal Society of Chemistry 2017

that the few-layer MoS_2 nanosheets decorated core/shell Ni_3-S_2@MoS_2 coaxial nanofibers enhanced the electrochemical activity of the active materials, attributed to the synergistic contribution of the homogeneous atomic heterointerface and the "stacking card" structure derived from the assembly of MoS_2 nanosheets. A yolk–shell SnS–MoS_2 composite was transformed by Sn–Mo oxide yolk–shell microspheres.[127] The discharge capacity of the yolk–shell SnS–MoS_2 composite microspheres for the 100th cycle was 396 mA h g^{-1} with a capacity retention of 89% compared with that in the 2nd cycle. The synergetic effect of the yolk–shell structure and uniform mixing of the SnS and MoS_2 nanocrystals resulted in excellent Na$^+$ ion storage properties by improving their structural stability during cycling.

Surface passivation of 2D nanosheets of MoS_2 can significantly improve the cyclic performance of SIBs.[128] Alshareef et al. reported coating MoS_2 nanosheets with a nanoscale layer of HfO_2 using an atomic layer deposition technique to form a MoS_2/HfO_2 composite and its use as an SIB anode material. At a current density of 100 mA g^{-1}, the initial discharge capacity of the MoS_2/HfO_2 composite was 1058 mA h g^{-1} which is quite close to that of the bare MoS_2 electrode. However, the cyclic performance was tremendously improved, and after 50-cycles the MoS_2/HfO_2 electrode retained 91% of its second discharge capacity. This capacity retention was much higher than that of the bare MoS_2. This capacity improvement was attributed to the passivation nature of the HfO_2 layer, which acted as a secondary electrolyte layer suppressing sulfur dissolution during the charge/discharge process. Furthermore, the amorphous layer of HfO_2 facilitated Na$^+$ ion diffusion and did not create any barrier.

On the other hand, MoS_2 can work as an additive in the SIB electrode. In addition to the direct use as an active material, MoS_2 is also attractive as a conducting additive to modify other electrode materials for SIBs because of short paths enabling fast ion diffusion, large exposed surface, as well as abundant ion insertion channels. MoS_2 was reported to modify the surface of the TiO_2 and spinel $Li_4Ti_5O_{12}$ electrode materials of SIBs.[129,130] TiO_2-B/MoS_2 nanowire arrays with a core–shell structure were directly fabricated on a current collector and explored as additive-free SIB anodes.[129] This self-supported 1D nanostructure was particularly interesting, owing to its vertical ion- and electron-transport properties and its ability to accommodate sodiation induced stresses. While the TiO_2-B nanowire array offered good cycling stability, the MoS_2 film offered high capacity and superior conductivity with excellent charge distribution throughout the film. The TiO_2-B/MoS_2 electrode retained a charge capacity of 191 mA h g^{-1} after 100 cycles, which is much higher than that of 112 and 103 mA h g^{-1} observed for the TiO_2-B and MoS_2 electrodes under the same conditions, respectively. MoS_2 quantum dots (QDs) and $Li_4Ti_5O_{12}$ nanosheets formed a heterostructured composite through a self-assembly process.[130] As anode materials of SIBs, the polarization between the charging and discharging plateaus of the $Li_4Ti_5O_{12}$–MoS_2 QD composite electrode was smaller than that of the bare $Li_4Ti_5O_{12}$ nanosheets, indicating better rate capability. At rates of 2 and 5C, the capacities of the composite electrode were 118 and 91 mA h g^{-1} and greater than those of the $Li_4Ti_5O_{12}$ electrode, 73 and 49 mA h g^{-1}, respectively. For the $Li_4Ti_5O_{12}$–MoS_2 QD

electrode, at 2C, a capacity of 101 mA h g^{-1} was retained after 200 cycles, which was superior to that (60 mA h g^{-1}) of the $Li_4Ti_5O_{12}$ nanosheets. The superior Na storage performance of the $Li_4Ti_5O_{12}$/MoS_2 heterostructure composite can be attributed to enhancement in the transport kinetics of the electrode based on the electrochemical impedance spectra analysis.

2.2 $MoSe_2$ nanostructure electrodes

$MoSe_2$, similar to MoS_2, with a sandwich structure, is composed of stacked atom layers (Se–Mo–Se) held together by van der Waals force. Featuring larger space between adjacent layers and a smaller band gap,[131] which are expected to contribute to higher CE and electronic conductivity, $MoSe_2$ can be used as a promising anode material in LIBs or SIBs with a similar energy storage mechanism to MoS_2.

Tirado et al. demonstrated the possibility of Na$^+$ ion intercalation in $MoSe_2$ based on an intercalation–deintercalation reaction mechanism.[132] Recently, much work has been done on $MoSe_2$ as a SIB anode. Jiang and coworkers have prepared $MoSe_2$ nanoplates and $MoSe_2$ nanospheres using a pyrolysis process and solvothermal reaction, respectively.[133,134] As a SIB anode, the $MoSe_2$ nanoplates were capable of delivering initial discharge and charge capacities of 513 and 440 mA h g^{-1} at a current of 0.1C in the voltage range of 0.1–3 V, respectively.[133] The electronic structure, Na$^+$ ion transport and conductivity were investigated by first-principles calculation. A quasi-2D energy favorable trajectory was proposed to illustrate the Na$^+$ ion vacancy-hopping migration mechanism from an octahedron to a tetrahedron in the $MoSe_2$ lattice. The unique $MoSe_2$ nanospheres rendered high-rate transportation of Na$^+$ ion due to its small size and high specific surface area.[134] As a SIB anode, $MoSe_2$ nanospheres delivered initial discharge/charge capacities of 520/430 mA h g^{-1} in the voltage range of 0.1 to 3 V at a current of 42.2 mA g^{-1} with an 80% capacity retention after 200 cycles.

$MoSe_2$ nanocomposites with porous hollow carbon spheres (PHCS) were prepared and used as anode materials.[135] The sodium storage performances of $MoSe_2$@PHCS and $MoSe_2$ nanosheets were measured and compared. The $MoSe_2$@PHCS composite exhibited enhanced cycling stability compared with the $MoSe_2$ nanosheets (Fig. 9). From the second cycle onwards, the $MoSe_2$@PHCS composite manifested a capacity of 580 mA h g^{-1} after 100 cycles. For comparison, $MoSe_2$ nanosheets exhibited much faster capacity fading after 60 cycles and only 100 mA h g^{-1} was retained after 100 cycles. The enhanced electrochemical performance of the $MoSe_2$@PHCS should be attributed to the synergic effects between the hollow porous carbon spheres and $MoSe_2$ nanosheets at the nanoscale. Core–shell MoS_2/C nanospheres embedded in foam-like carbon sheets were fabricated by a facile glucose carbonization process.[136] The 300th discharge capacity could reach 337 mA h g^{-1} at current density of 1 A g^{-1}. The superior electrochemical performance can be attributed to the carbon coated MoS_2 nanospheres in the carbon matrix.

Recently, Kang et al. also carried out studies on $MoSe_2$ as the anode for SIBs.[137,138] They prepared yolk–shell-structured $MoSe_2$
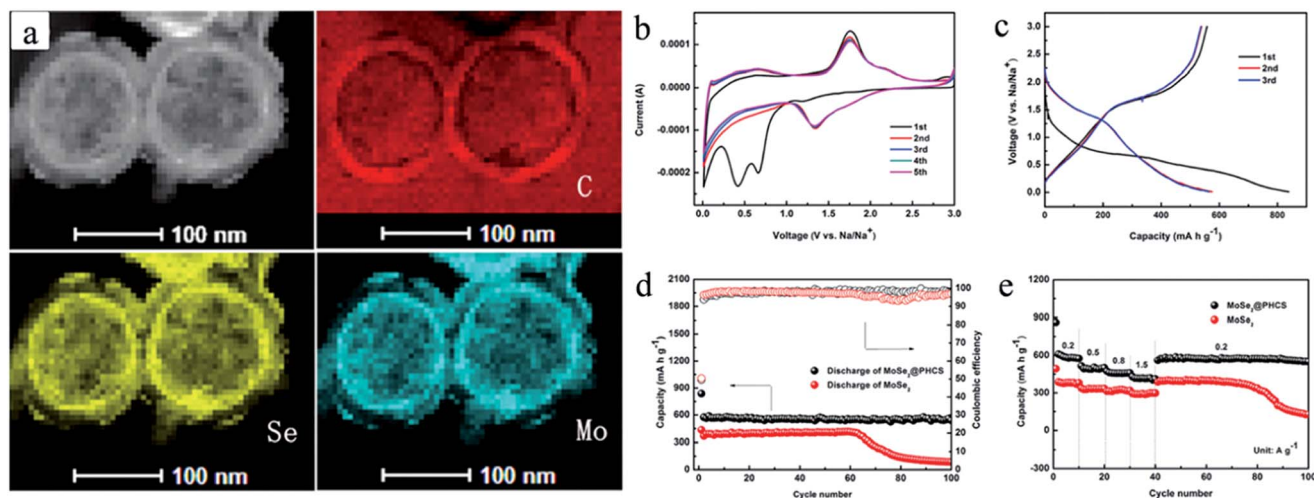
This journal is © The Royal Society of Chemistry 2017

J. Mater. Chem. A, 2017, **5**, 7667–7690 | 7679

Fig. 9 (a) Elemental mapping images of the $MoSe_2@$ PHCS composite. (b) Cyclic voltammogram profiles at a scan rate of 0.2 mV s^{-1} and (c) discharge/charge voltage profiles at a current density of 200 mA g^{-1} for the $MoSe_2@$PHCS composite. (d) Cycling performance and CE at a current density of 200 mA g^{-1}. (e) Rate performance. Reprinted with permission from ref. 135, Copyright (2015) by The Royal Society of Chemistry.

microspheres *via* a simple selenization process of MoO_3 microspheres.[137] The yolk–shell-structured $MoSe_2$ and MoO_3 microspheres delivered initial discharge capacities of 527 and 465 mA h g^{-1}, respectively, in the voltage range of 0.001–3 V *vs.* Na/Na$^+$ at 0.2 A g^{-1}. Their discharge capacities were found to be 433 and 141 mA h g^{-1} after 50 cycles, respectively. The hierarchical yolk–shell structure comprised of wrinkled nanosheets facilitated fast Na-ion and electron kinetics, and buffered the large volume changes encountered during conversion-type cycling. They also fabricated 3D porous-structured CNT balls embedded with fullerene-like $MoSe_2$ nanocrystals (F–$MoSe_2$/CNTs) by the spray pyrolysis process and subsequent selenization process.[138] The cycling performance of the F–$MoSe_2$/CNT composite balls was found to be better than those of bare $MoSe_2$ and the N–$MoSe_2$/CNT composite balls. The 250th discharge capacities of bare $MoSe_2$, the N–$MoSe_2$/CNT composite balls, and the F–$MoSe_2$/CNT composite balls were 144, 200, and 296 mA h g^{-1}, respectively, at a high current density of 1.0 A g^{-1}, and their capacity retentions measured from the second cycle were 37%, 66%, and 83%, respectively. The synergetic effect of the F–$MoSe_2$ nanocrystals with ultrafine sizes and the CNT balls with the tangled and 3D porous structure and high electrical conductivity resulted in excellent Na-ion storage properties of the F–$MoSe_2$/CNT composite balls. Highly crystalline $MoSe_2@$-multi-walled carbon nanotube composites ($MoSe_2@$MWCNTs) were obtained from a one-step hydrothermal method and a subsequent calcination process.[139] The $MoSe_2@$MWCNT composites exhibited excellent electrochemical performance as anode materials for sodium storage, which could deliver a reversible specific capacity of 459 mA h g^{-1} at a current of 200 mA g^{-1} over 90 cycles, and a specific capacity of 385 mA h g^{-1} at a high current of 2000 mA g^{-1}. Employing MWCNTs as templates offered a beneficial conductivity environment. The uniform and conformal ultrathin $MoSe_2$ nanosheets shorten the pathway of ions and electrons.

A C–$MoSe_2$/rGO composite with both high porosity and large surface area can be obtained through double modification of $MoSe_2$ nanosheets by introducing an rGO skeleton and an outer carbon protective layer.[140] The $MoSe_2$ nanosheets were well wrapped by a carbon layer and also strongly anchored on the interconnected rGO network. As an SIB anode, the designed C–$MoSe_2$/rGO composite delivered noticeably enhanced Na$^+$ ion storage capability, with a high specific capacity of 445 mA h g^{-1} at 200 mA g^{-1} after 350 cycles, and 228 mA h g^{-1} even at 4 A g^{-1}; these values were much better than those of C–$MoSe_2$ nanosheets (258 mA h g^{-1} at 200 mA g^{-1} and 75 mA h g^{-1} at 4 A g^{-1}). The $MoSe_2$/carbon fiber flexible electrode can be fabricated by a solvothermal reaction.[141] It can deliver a stable discharge capacity of 452.6 mA h g^{-1} and exhibit 85.5% retention after 100 cycles at 0.2 A g^{-1}, and achieve a high capacity of 161.9 mA h g^{-1} even at a high current of 5 A g^{-1}.

In addition to MoS_2 and $MoSe_2$, layered $MoTe_2$ nanostructures are also a promising host for sodium storage. $MoTe_2$ possesses a similar structure to MoS_2, but an even larger interlayer spacing of 0.699 nm. Very recently, a C–$MoTe_2$ composite microsphere anode was prepared through tellurization of a C–MoO_x composite. At 1.0 A g^{-1}, the discharge capacity of the C–$MoTe_2$ for the 200th cycle was 286 mA h g^{-1} with a capacity retention of 99% compared with that in the 2nd cycle attributed to the high structural stability and well-developed two-dimensional layer of $MoTe_2$ in microsphere structures.[142]

3. WS$_2$ nanostructures as SIB anodes

WS_2 has a large interlayer spacing of 6.18 Å along the *c*-axis, which can accommodate the large Na$^+$ ions. The interactions between WS_2 layers are relatively weaker than those of MoS_2, which should make Na$^+$ ion much easier to intercalate. Furthermore, WS_2 has a higher intrinsic conductivity than MoS_2.[143,144] Therefore, it is an ideal anode candidate for SIBs.

Well-designed WS_2 nanostructures have been reported to be favorable for anode performance in SIBs.

WS_2 nanowires with a very thin diameter of 25 nm and an expanded interlayer spacing of 0.83 nm were prepared by using a facile solvothermal method followed by a heat treatment, which offered good electrochemical accessibility and open channels for rapid Na^+ ion intercalation/deintercalation.[145] WS_2 nanowires displayed remarkable capacity (605.3 mA h g^{-1} at 100 mA g^{-1}) but inferior cyclability in the voltage range of 0.01–2.5 V. However, by limiting the cut-off voltage to 0.5 V, only the intercalation mechanism took place and the conversion reaction could be avoided. In this case, the nanowire-framework was well preserved, and the WS_2 layers were gradually expanded and exfoliated during prolonged electrochemical cycling, which would produce more active sites for Na^+ ion storage, and also can facilitate the electronic and ionic diffusion kinetics. Thus, WS_2 NWs exhibited an excellent stability of 1400 cycles with a considerable capacity of 330 mA h g^{-1} at 1000 mA g^{-1}.

WS_2@graphene nanocomposites have always been studied as SIB anode materials. Su *et al.* prepared WS_2@graphene nanocomposites by a hydrothermal approach.[146] When applied as anode materials in SIBs, the WS_2@graphene nanocomposite showed a highly reactive nature towards sodium storage. It demonstrated a high reversible specific capacity of about 594 mA h g^{-1}, excellent cyclability, and good high rate performance, which could be ascribed to the highly conductive graphene matrix and the unique 3D architecture of the nanocomposite. Layered WS_2-3D rGO microspheres were prepared using two steps including spray pyrolysis and sulfidation process.[147] The WS_2-3D rGO microspheres sulfidated at 400 °C showed Na^+ ion storage properties superior to those of similarly structured WO_3-3D rGO microspheres. The discharge capacity of the WS_2-3D rGO microspheres at the 200th cycle was 334 mA h g^{-1}. The capacity retention of the WS_2-3D rGO microspheres measured from the second step was as high as 93%, and the CE remained stable at 99.92% after the 10th cycle. A 3D porous interconnected WS_2/C nanocomposite was prepared by an electrostatic spray deposition technique, which was composed of nano-0D WS_2, nano-1D CNTs and nano-2D rGO.[148] Such a WS_2/C nanocomposite was demonstrated to work as a promising anode for SIBs. It can deliver a reversible capacity of ~400 mA h g^{-1} at 0.2C. When the current densities were increased to 1C, 2C and 10C, the capacity still remained at high values of 270, 199 and 81 mA h g^{-1}, respectively, indicating outstanding rate performance. It also exhibited an excellent cycling stability. At a current density of 1C, the capacity was as high as 219 mA h g^{-1} after 300 cycles. The superior electrochemical performance (*i.e.* high rate capability and long cycling stability) was due to the unique 3D porous interconnected WS_2/C nanocomposite. Firstly, the small size of WS_2 nanodots was beneficial for the transport of electrons and Na^+ ions, resulting in efficient Na^+ ion storage. Secondly, the 3D porous interconnected structure constructed using rGO and CNTs offered fast electron transporting channels, and buffered the volume change during cycling. Thirdly, such a porous structure favored electrolyte penetration and allowed for better contact and fast Na ion transport. Last but not least, the WS_2/C nanocomposite

obtained through the electrostatic spray deposition technique can be directly deposited on the current collectors without binders and conductive carbons, simplifying the battery fabrication process. WS_2/CNT–rGO aerogels with an ordered micro-channel 3D structure were synthesized through a simple solvothermal method and ice-template assisted post-freeze drying process. The nanocomposite can deliver specific capacities of 311.4 mA h g^{-1} at 100 mA g^{-1} in SIBs. The excellent electrochemical performance has been attributed to the synergistic effect between the WS_2 nanosheets and CNT–rGO network, and the specially designed unique 3D ordered microchannel nanoarchitectures.[149]

Heterogeneous electrode materials with hierarchical architectures are promising for considerable improvement in future energy storage devices.[150] Heterogeneous tungsten sulfide/oxide core–shell nanofiber materials with vertically and randomly aligned thorn-bush features were prepared through a simple thermal treatment of WS_x in air as shown in Fig. 10. The heterogeneous thorn-bush nanofiber electrodes delivered a high second discharge capacity of 791 mA h g^{-1} and improved cycle performance for 100 cycles compared to the pristine WS_x and WO_3 nanofibers. The extended surface area of the thorn-bush nanofibers as a result of nanobranch formation provided more reaction sites for Na^+ ions, and the thin layer of WO_3 on the WS_x nanofiber backbone can effectively maintain the kinetic performance. Sulfur components can be observed in the cycled Na counter electrodes obtained from the cells employing WS_x as an electrode, while there is no obvious sulfur component in Na counter electrodes in the WS_x/WO_3 cells (Fig. 10f). This reveals that oxide surface layer modification on the WS_x nanofiber electrode can effectively alleviate sulfur dissolution. High capacity and improved cycle performance of SIB anodes can be simultaneously achieved by the introduction of hierarchical sulfide nanofiber materials with oxide surface features.

Besides, carbon-coated WSe_2 with a similar crystal structure to WS_2 has been synthesized and used in SIBs. 75.57% crystal WSe_2 nanoparticles were uniformly dispersed on a carbon matrix to form WSe_2/C nanocomposites. They can exhibit high discharge capacity and excellent cycling stability, attributed to the buffering effect of the carbon matrix and improved conductivity of the composites.[151]

4. Sn-based anodes for SIBs

4.1 Sodium storage mechanism of SnS_2

Tin-based compounds have attracted considerable attention and have been investigated as anode materials for SIBs due to their high theoretical capacities and low working voltage.[152–164] Tin has a theoretical capacity of 847 mA h g^{-1} in the alloying reaction resulting in the formation of $Na_{15}Sn_4$. Considering the additional capacity contribution from the conversion reaction, tin oxides and sulfides possess higher theoretical capacities compared to metallic tin. Moreover, tin sulfides appear to be more promising due to their superior delivered performance, receiving increasing scientific attention. Tin sulfides can also theoretically combine the well-known Na–S conversion reaction with an alloying reaction to yield a high capacity anode that
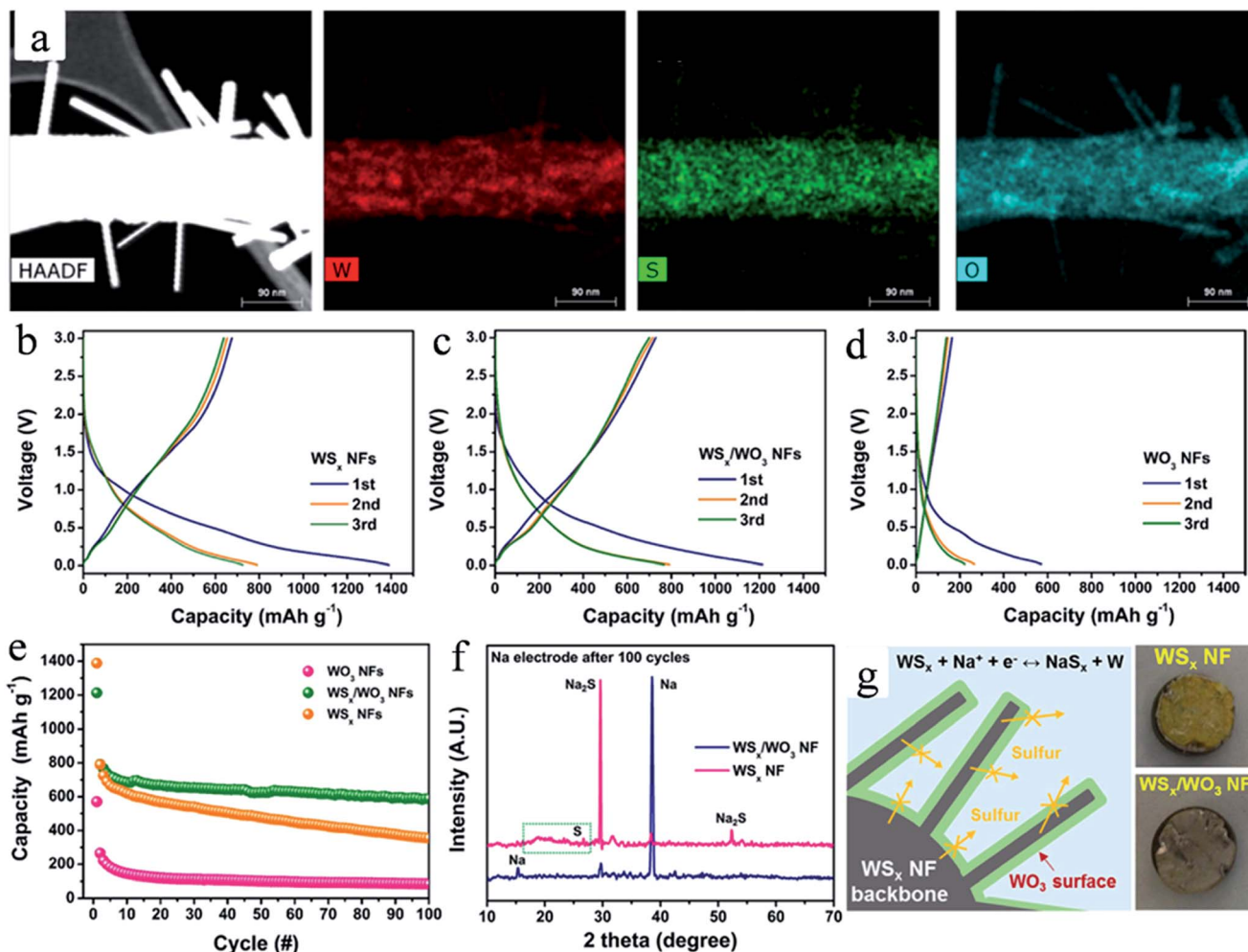
This journal is © The Royal Society of Chemistry 2017

J. Mater. Chem. A, 2017, **5**, 7667–7690 | **7681**

Fig. 10 (a) HAADF image of postcalcined WS$_x$ nanofibers at 400 °C in air and element maps of tungsten, sulfur, and oxygen; charge/discharge voltage curves of (b) the pristine WS$_x$ nanofibers and the postcalcined WS$_x$ nanofibers at (c) 400 and (d) 500 °C. (e) Cycle performance of the WS$_x$ nanofibers and the postcalcined WS$_x$ nanofibers at 400 and 500 °C at a current density of 100 mA g^{-1}; (f) *ex situ* XRD patterns of the electrodes after 100 cycles; (g) schematic illustration of the reaction mechanism during cell operation and photos of Na counter electrodes. Reprinted with permission from ref. 150, Copyright (2016) by American Chemical Society.

effectively operates as S–Na and Sn–Na nanocomposites (the SnS$_2$ does not re-form upon desodiation). For hexagonal SnS$_2$, the reactions are the following: SnS$_2$ + Na$^+$ + e$^-$ → NaSnS$_2$, NaSnS$_2$ + 3Na → Sn + 2Na$_2$S and Sn + 3.75Na → Na$_{15}$Sn$_4$, yielding a reversible capacity of 1137 mA h g^{-1}.[162] The ortho-rhombic SnS phase undergoes an analogous reaction: SnS + 2Na → Sn + Na$_2$S and Sn + 3.75Na → Na$_{15}$Sn$_4$, giving a theoretical capacity of 1022 mA h g^{-1}. To enhance the cycling stability, well-designed SnS$_2$ nanostructures could better accommodate large volume variation during the Na-alloying reaction as well as provide a better Na$^+$ ion diffusion pathway.

An excellent comparison of the performance between SnS$_2$ and SnS was recently published by Guo *et al.*[159] They employed a tin sulfide/graphene architecture and demonstrated that both the sulfide materials decomposed to metallic Sn, which was consequently alloyed to form the intermetallic Na$_{15}$Sn$_4$. In the case of SnS, the decomposed Sn phase had a diamond cubic crystal structure (low temperature α-tin). In the case of SnS$_2$, the decomposed Sn phase had a tetragonal crystal structure

(metallic β-tin). Based on the cyclic voltammetry profiles, they argued that the SnS phase was reformed during desodiation, while SnS$_2$ remains permanently decomposed. However, the *ex situ* XRD patterns collected during the first desodiation did not display the characteristic SnS Bragg reflections, rather they showed clear S and Sn (separate analysis) signals.

4.2 SnS$_2$ nanosheets

Considering the higher theoretical capacity, SnS$_2$ has a CdI$_2$-type of layered structure (a = 0.3648 nm, c = 0.5899 nm, space group $P3m1$) consisting of a layer of tin atoms sandwiched between two layers of hexagonally close packed sulfur atoms. This layered structure with a large interlayer spacing of 0.5899 nm along the c axis should be in favor of insertion and extraction of guest species and more easily endure the volume changes in the host during cycling. This has been confirmed by the performance of SnS$_2$ as a reversible lithium storage host in several studies.[165–168] SnS$_2$ is a more competitive anode material

7682 | *J. Mater. Chem. A*, 2017, 5, 7667–7690

This journal is © The Royal Society of Chemistry 2017

for high-performance sodium storage. Ultrathin 2D SnS_2 nanosheets (3–4 nm in thickness) were synthesized *via* a facile reflux process based on an Ostwald ripening process, in which low-energy facets were exposed to reduce the surface energy.[169] As anode materials for SIBs, the SnS_2 nanosheets delivered a high reversible specific capacity of 733 and 435 mA h g^{-1} at 0.1 and 2 A g^{-1}, respectively, and still maintained a capacity as high as 647 mA h g^{-1} during the 50th cycle at 0.1 A g^{-1}, indicating excellent rate and cycling performance. The excellent performance can be attributed to the unique ultrathin morphology of SnS_2 nanosheets, which was beneficial to achieve fast sodiation/desodiation kinetics and to accommodate electrode volume change. Even in a full cell combined with a $Na_3V_2(PO_4)_3$ cathode, the anode successfully demonstrated impressive performance.

4.3 SnS_2/graphene nanocomposites

The electrochemical properties of layered sulfides (SnS_2, MoS_2, WS_2) were always further improved by integration with graphene. The structural compatibility between the layered compounds and the good electronic properties of graphene led to the formation of very stable composites with high reversible capacity and good rate performance in LIB applications.[170–173] The SnS_2 layered structure should also be viable for reversible Na^+ ion storage in comparison with tin and other tin-based materials, since it can buffer the volume changes well in Na–Sn reactions. The successful developmental efforts towards LIBs also validate SnS_2–rGO nanocomposites as an improved SIB anode material.[160–162,164,174–180]

Lee's group has proposed a novel SnS_2–rGO composite anode with excellent electrochemical performance for SIBs.[160] The SnS_2–rGO electrode demonstrated high reversible capacity (630 mA h g^{-1} at 0.2 A g^{-1}), good rate performance (544 mA h g^{-1} at 2 A g^{-1}), and long cycle-life (500 mA h g^{-1} at 1 A g^{-1} after 400 cycles). Obviously, the SnS_2 should first undergo a conversion reaction with Na to form Sn and Na_2S. Then Sn should further alloy with Na to form the $Na_{15}Sn_4$ alloy phase. Furthermore, the authors continued a more in-depth study on the energy storage mechanism of the SnS_2–rGO composite to reveal a sophisticated reaction pathway.[180] The structural evolution and phase transformation of the electrode upon discharge/charge are tracked by SXRD, XAS, TEM, and Raman spectroscopy, confirming that Sn appears as an intermediate product which is then converted into $Na_{15}Sn_4$ and Na_2S_2 rather than Na_2S in the final reaction product. The SnS_2 became amorphous upon insertion/removal of Na^+ ion after a full cycle. The synergistic mechanism that took advantages of both conversion and alloying reactions ensured the high specific capacity, long cycle life, and fast kinetics. The rGO allowed for effective dispersion of the pristine SnS_2 particles and prevented the agglomeration of the nano-sized reaction products. Benefiting from both the synergistic effect and the assistance of rGO, highly efficient and durable sodium storage was achieved by this SnS_2–rGO anode in SIBs. The unique plate-on-sheet structure composed of ultrafine (<10 nm), few-layered (≤7 layers) SnS_2 and few-layered rGO (<6 layers) yielded charge capacities of 507 and 360 mA h g^{-1},

respectively, after 300 cycles at 200 mA g^{-1} and 500 cycles at 400 mA g^{-1}.[161] The hybrid can sustain 1000 cycles under 800 mA g^{-1} (1.8C), maintaining a capacity around 300 mA h g^{-1}. The ultralong cycle life of SnS_2/rGO was attributed to the buffering effect of the flexible rGO and the free space in the hybrid. Besides, the formation of a stable SEI film also contributed to the excellent cycling performance by stabilizing the electrode/electrolyte interface. The hybrid can yield high rate capacities of 524, 501, and 452 mA h g^{-1}, respectively, at high current densities of 1.6, 3.2, and 6.4 A g^{-1}. Even at 12.8 A g^{-1} (28C), it can deliver a moderate charge capacity of 337 mA h g^{-1}. The excellent rate capability was ascribed to 2D conductive channels constructed by rGO, the small lateral size and ultrathin nature of layered SnS_2, the unique hybrid structure with enhanced electrolyte penetration, and rapid Na^+ ion transport. It was supposed that a more open-framework structure with few-layer sheets can facilitate the transportation of Na^+ ions and ensure the flooding of the electrolyte. Xiong's group reported ultrasmall SnS_2 nanoparticles anchored on well distributed nitrogen-doped or amino-functionalized graphene, showing enhanced cycling stability.[174,175] Well-distributed graphene sheets doped with nitrogen (NGSs) were prepared *via* a thermal annealing strategy with the use of cyanamide.[173] Following the next-step of the low-temperature solvothermal route, uniform ultrasmall SnS_2 nanocrystals were readily grown on the pre-formed NGS (denoted as SnS_2–NGS). Benefiting from the synergistic function between NGSs and SnS_2, the resultant composites exhibit excellent electrochemical performance. A capacity of about 450 mA h g^{-1} can be achieved at 200 mA g^{-1} after 100 cycles. At 10 A g^{-1}, the capacity can also reach 148 mA h g^{-1}. Then the authors proposed a facile approach for binding SnS_2 nanocrystals through C–N–Sn bonding on EDA-functionalized rGO sheets to achieve SnS_2 nanocrystal/EDA-functionalized rGO composites (SnS_2 NC/EDA–rGO) (Fig. 11).[175] The long-term cycling test was first activated at 200 mA g^{-1} for 5 cycles and then cycled at 1 A g^{-1} for 1000 cycles. The discharge capacity at the 1000th cycle at 1 A g^{-1} was 480 mA h g^{-1}, which was 85% of that at the 10th cycle. Under the same conditions, the discharge capacity of SnS_2/rGO at the 1000th cycle was only 255.6 mA h g^{-1}, corresponding to a capacity retention of only 43.8%. The combination of ultrafine SnS_2 nanocrystals and highly conductive graphene synergistically enhanced the ion and charge transfer kinetics of the SnS_2 NC/EDA–rGO nanocomposite. What's more, the vigorous chemical interaction on the SnS_2 NC/EDA–rGO interface derived from the EDA's bridging role between nanocrystals and nanosheets, as well as the discharge products, can effectively strengthen physicochemical interactions, and hence essentially improve the reversible capacity, rate profile and cycling performance. Furthermore, SnS_2, exfoliated by the hydrolysis of lithiated SnS_2 ($LiSnS_2$) restacked on graphene, was prepared through a cetyltrimethyl ammonium bromide-assisted hydrothermal method.[164] It was found that the obtained SnS_2/graphene nanocomposite exhibited excellent electrochemical properties in SIBs, delivering a remarkable capacity as high as 650 mA h g^{-1} at a current of 200 mA g^{-1}. More impressively, the capacity can reach 326 mA h g^{-1} even at 4000 mA g^{-1} and

This journal is © The Royal Society of Chemistry 2017

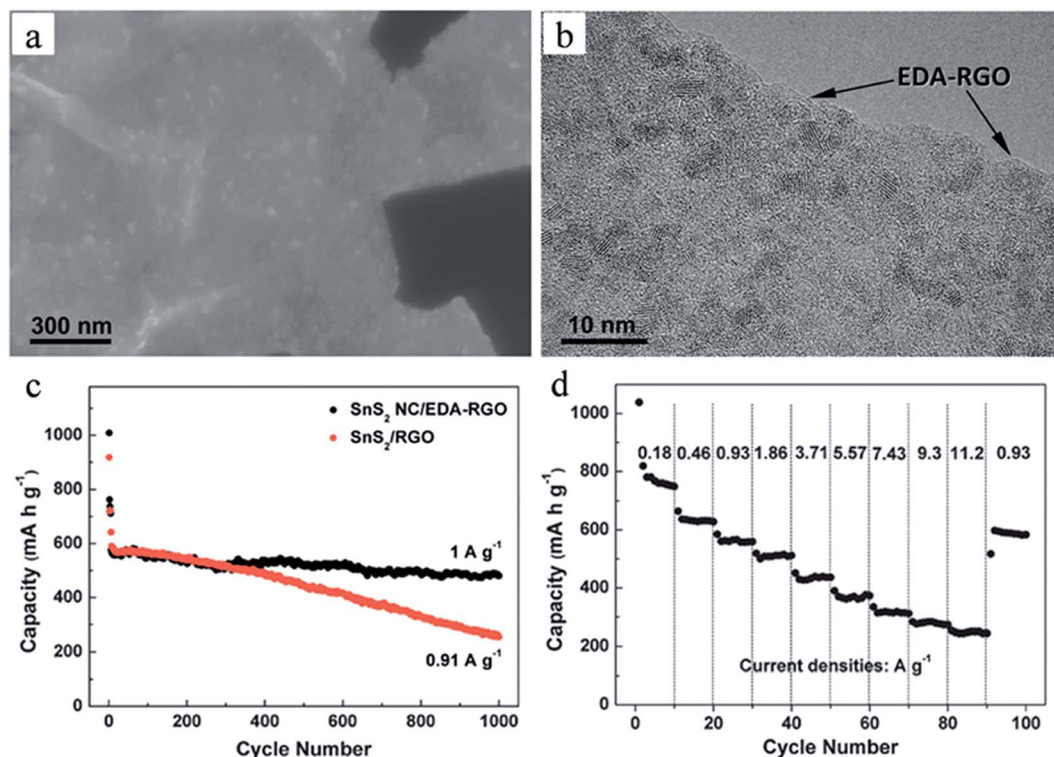*J. Mater. Chem. A*, 2017, **5**, 7667–7690 | **7683**

Fig. 11   (a) High-magnification FESEM and (b) HRTEM image of SnS_2 NC/EDA−rGO. (c) Cycling performance of the SnS_2 NC/EDA−rGO anode at a current density of 1 A g^{-1}, in comparison with a SnS_2/rGO anode. (d) The discharge capacities at different current densities of the SnS_2 NC/EDA−rGO anode. Reprinted with permission from ref. 175, Copyright (2016) by The Royal Society of Chemistry.

remain stable at about 610 mA h g^{-1} without fading up to 300 cycles when the rate returned to 200 mA g^{-1}. The tiny SnS_2 nanoplates (20–50 nm in size) composed of 2–5 layers, as well as the few enlarged interlayer spacings, were readily accessible to the electrolyte, which can facilitate the reversible Na$^+$ ion diffusion kinetics, thus ensuring full utilization of active materials with a high capacity. Second, the introduction of the N-doped graphene matrix can provide a 3D conductive network and effective buffering for volume fluctuation, and decrease the aggregation of active materials during the cycling process.

4.4 SnS_2/carbon nanocomposites

Other carbon materials (amorphous carbon and CNTs) have also been integrated with SnS_2 to work as efficient anodes for SIBs. A SnS_2/C anode material was synthesized by annealing Sn, sulfur powder, and polyacrylonitrile in a sealed vacuum glass tube.[176] The SnS_2/C nanospheres with a unique layered structure exhibited a high reversible capacity of 660 mA h g^{-1} at a current density of 50 mA g^{-1} and maintained at 570 mA h g^{-1} after 100 cycles with a degradation rate of 0.14% per cycle. The superior cycling stability of the SnS_2/C electrode was attributed to the stable nanosphere morphology and structural integrity during charge/discharge cycles as evidenced by *ex situ* characterization. A hybrid nanostructure with SnS_2 cross-linked by the CNTs demonstrated an ultrahigh capacity of 758 mA h g^{-1} at 100 mA g^{-1} and superior rate performances (445 mA h g^{-1} at 5 A g^{-1}) and long cycle life (87% capacity retention after 300 cycles at 1 A

g^{-1}).[179] The superior electrochemical performances could be attributed to the unique nanostructure consisting of the 2D SnS_2 sheets and 1D criss-cross CNTs, which provided multiple dimension pathways for the electron and ion transport, thus resulting in enhanced conductivity. On the other hand, the strong mechanical properties of the CNTs enabled a robust structure to alleviate the volume expansion during cycling. Growing SnS_2 nanosheet arrays directly on carbon fiber cloth, followed by wrapping the SnS_2 nanosheets with graphene nanosheets can deliver a reversible specific capacity as high as 378 mA h g^{-1} after 200 cycles.[177]

Besides, SnS possesses a layered structure and was also studied as an anode material for SIBs. Wu and co-workers examined Sn–SnS–C nanocomposites as SIB anodes and reported reversible capacities of 664 mA h g^{-1} at 20 mA g^{-1} and 350 mA h g^{-1} at 800 mA g^{-1}.[153] A 3D porous interconnected metal sulfide/carbon (SnS:C) nanocomposite was prepared by the electrostatic spray deposition technique.[158] Small nanorods of SnS are generated with sizes of ~10–20 nm embedded in amorphous carbon and self-assembled into a 3D porous interconnected nanocomposite. The discharge capacities are 419, 334, 310, 205, and 145 mA h g^{-1}, respectively, when current densities of 100, 500, 1000, 5000, and 10 000 mA g^{-1} are applied. At a current density of 1 A g^{-1}, after 300 cycles more than 80% discharge capacity was still retained with almost ≈100% CE. The superior electrochemical performance is attributed to three reasons: (i) the tiny dimensions of the SnS particles were beneficial for energy storage by improving the

7684 | J. Mater. Chem. A, 2017, 5, 7667–7690

This journal is © The Royal Society of Chemistry 2017

transport of both electrons and ions; (ii) uniformly coated carbon pronouncedly increased the electronic conductivity of the SnS:C; (iii) the 3D porous interconnected structure not only effectively buffered the volume change during cycling, but also provided many channels to give access to the electrolyte, which was facile for ion transport.

5. Other MX$_2$ electrodes

5.1 Other layered MX$_2$

Besides MoS$_2$ and WS$_2$, layered TiS$_2$ and VS$_2$ are two typical family members of transition-metal dichalcogenides, which have been investigated as host materials for sodium storage. In 1976, Winn et al. first reported that Na$^+$ ions in propylene carbonate could be electrochemically intercalated into TiS$_2$ single crystals using coulometric titrations.[181] Reversible room-temperature Na/TiS$_2$ cells were successfully demonstrated by Newman et al. In 1980, however, they were found to suffer from rapid capacity fading upon cycling, especially in the high potential region.[31] These early studies were followed by many subsequent efforts to improve their electrochemical performance.[182–184] However, about 40 years later, there is still no available solution to stabilize TiS$_2$ for fast Na$^+$ ion storage. Based on the DFT study, it was concluded that the diffusion kinetics of Na$^+$ ions would benefit from the nanostructure design of TiS$_2$, which can shed light on their prospect as SIB electrode materials.[185] Recently, Liu et al. reported the preparation of thin TiS$_2$ nanoplates as the cathode material of SIBs.[186] These nanoplates possessed nanoscale dimensions and large surface areas. Their interlayer galleries were open toward the edges, providing easy access to the large internal-space. Electrochemical measurements and multiple ex situ studies demonstrated that TiS$_2$ nanoplates were capable of fast and reversible Na$^+$ ion intercalation and deintercalation. They delivered a large capacity close to full Na$^+$ ion intercalation (186 mA h g^{-1}), high rate capability (100 mA h g^{-1} at 10C) and satisfactory cycling stability at both low and high current rates.

VS$_2$ was first discovered in the 1970s. DFT calculation reveals that VS$_2$ monolayers show metallic behavior.[187] Kuo's group have investigated the capability of monolayer VS$_2$ polytypes as potential anode materials for SIBs via DFT coupled to an ab initio random structure search.[188] Liao et al. prepared VS$_2$ nanosheets coated Na$_2$Ti$_2$O$_5$ nanowire arrays on flexible Ti foil as an additive-free 3D anode for SIBs.[189] Notably, after modification with VS$_2$, these unique 3D nanowire array anodes demonstrated superior electrochemical performance including high charge/discharge capacities, improved capability, and exemplary cycling performance.

Owing to the merits of layered structures with large interlayer spacings facilitating ion intercalation and extraction, various MX$_2$ compounds are promising as host materials for sodium storage. Na$^+$ ion adsorption and migration in the layered CrS$_2$, CoTe$_2$, NiTe$_2$, ZrS$_2$ and NbS$_2$ are predicted using first-principles calculations.[190] Application of layered ReS$_2$ in LIBs with excellent cycling stability has been recently demonstrated.[191] These layered MX$_2$ materials could be explored as new anode materials for SIBs in the near future.

5.2 Non-layered MX$_2$

In addition to the aforementioned layered MX$_2$, non-layered MX$_2$ nanostructures such as FeS$_2$, FeSe$_2$, CoS$_2$, CoSe$_2$, and NiS$_2$ have also been explored extensively as anode materials for SIBs in the past decade. For example, FeS$_2$ microspheres have demonstrated high-rate capability (170 mA h g^{-1} at 20 A g^{-1}) and unprecedented long-term cyclability (~90% capacity retention for 20 000 cycles) by employing a compatible NaSO$_3$-CF$_3$/diglyme electrolyte and tuning the cut-off voltage to 0.8 V.[192] Co$_{0.5}$Fe$_{0.5}$S$_2$ nanospheres obtained from a solvothermal reaction had discharge capacities of 0.220 A h g^{-1} after 5000 cycles at 2 A g^{-1} and 0.172 A h g^{-1} even at 20 A g^{-1} in an ether-based electrolyte in a voltage window of 0.8–2.9 V.[193] A novel one-dimensional nanohybrid comprised of conductive graphitic carbon (GC)-coated hollow FeSe$_2$ nanospheres decorated rGO nanofiber demonstrated enhanced electrochemical properties due to the synergetic effects of the hollow morphology of FeSe$_2$ and the highly conductive rGO matrix.[194] CoS$_2$ nanoparticles (20–30 nm) anchored on rGO exhibited improved sodium storage. The CoS$_2$–rGO electrode delivered a reversible capacity of 192 mA h g^{-1} even after 1000 cycles at 1 A g^{-1}.[195] A CoS$_2$/MWCNT nanocomposite exhibited high capacity retention of 568 mA h g^{-1} after 100 cycles in an ether-based electrolyte.[196] Urchin-like CoSe$_2$ assembled by nanorods delivered a high capacity of 0.410 A h g^{-1} at 1 A g^{-1} after 1800 cycles between 0.5 and 3.0 V in an ether-based electrolyte.[197] NiS$_2$–graphene nanosheet composites exhibited superior capacity of 407 mA h g^{-1} with capacity retention of 77% over 200 cycles at a current density of 0.1C.[198] NiSe$_2$–rGO–C composite nanofibers were successfully prepared via an electrospinning process. This composite could maintain a 100th-cycle discharge capacity of 468 mA h g^{-1} at 200 mA g^{-1}.[199] Therefore, these non-layered MX$_2$ nanostructures can also show impressive electrochemical performance as anode materials for SIBs.

6. Summary and outlook

SIBs have been proposed as promising substitutes for LIBs, especially for large-scale stationary energy storage, considering the critical need to develop new batteries with high energy densities and low cost. Recently, plenty of breakthroughs have been achieved in improving the performance and safety of SIBs. However, their practical application critically depends on the electrode, especially the anode materials. Layered MX$_2$ can offer advantages of not only a large number of active sites for ion storage due to their high specific surface areas, but also shortened ion diffusion distances and fast ion transport due to the open 2D ion transport channel and thus are promising as electrode materials for SIBs.

In this review article, we have attempted to summarize recent progresses in nanostructured MX$_2$ as SIB anodes. MX$_2$ anodes still suffer from inferior kinetics and stability resulting from the unfavorable compatibility between the large intercalating ion and the limited lattice space available in the materials. As a result, a rational and creative design including nanostructure engineering, crystal structure and crystallinity,

hybrid structure with other materials and doping or alloying with other atoms can help conquer the drawbacks during the electrochemical reactions, thus dramatically enhancing the capacity, rate capability, and cycle life of the electrodes.

In the future, rational synthesis of MX_2-based anodes should be paid more attention to further develop some new structures with novel morphologies, various hybrids and doping, in order to enhance the structural stability and conductivity. In addition, the following issues should be paid more attention to in future research. First, large irreversible capacity has always been observed in the first cycle, which means that a large portion of Na^+ ions could not be utilized again in the following cycles when paired with a cathode in a full cell. Pre-sodiation treatments could be one of the strategies to minimize this problem, but more research efforts are necessary to overcome the above challenge. Second, to date, the use of $NaClO_4$ salt has been extensive and widespread. Other electrolytes such as $NaPF_6$, sodium bis(fluorosulfonyl)imide (NaFSI) and $NaSO_3CF_3$ have also been investigated as the Na salt. In addition to carbonate solvents, ethers are demonstrated to be helpful to enhance the sodium storage performance. Moreover, additives such as fluoroethylene carbonate (FEC) are found to improve the cyclability. Further exploration of the interface between the electrode and the electrolyte should be carried out with a modified design of electrolyte systems that could result in enhanced performances. Third, although conventional electrochemical characterization techniques, such as cyclic voltammetry, galvanostatic intermittent titration, electrochemical impedance spectroscopy, etc., are able to reveal the performance of bulk hybrid electrodes, they can hardly probe the intrinsic properties of the active material itself during ion insertion. MX_2 would be fabricated into nanoscale devices to probe their electron and thermal transport properties, and charge transfer characteristics from in situ observation. Thus, more research needs to be dedicated to understanding the underlying mechanisms of the changes induced in the behavior of MX_2 by ion intercalation, especially the electronic structure and charge transfer features.

Acknowledgements

References

1 A. S. Arico, P. Bruce, B. Scrosati, J. M. Tarascon and W. Van Schalkwijk, *Nat. Mater.*, 2005, **4**, 366–377.

2 B. Dunn, H. Kamath and J. M. Tarascon, *Science*, 2011, **334**, 928–935.

3 A. Manthiram, A. V. Murugan, A. Sarkar and T. Muraliganth, *Energy Environ. Sci.*, 2008, **1**, 621–638.

4 M. V. Reddy, G. V. Subba Rao and B. V. Chowdari, *Chem. Rev.*, 2013, **113**, 5364–5457.

5 Y.-G. Guo, J.-S. Hu and L.-J. Wan, *Adv. Mater.*, 2008, **20**, 2878–2887.

6 Z. Yang, J. Zhang, M. C. Kintner-Meyer, X. Lu, D. Choi, J. P. Lemmon and J. Liu, *Chem. Rev.*, 2011, **111**, 3577–3613.

7 M. Armand and J. M. Tarascon, *Nature*, 2008, **451**, 652–657.

8 P. G. Bruce, S. A. Freunberger, L. J. Hardwick and J. M. Tarascon, *Nat. Mater.*, 2012, **11**, 19–29.

9 G. N. Zhu, Y. G. Wang and Y. Y. Xia, *Energy Environ. Sci.*, 2012, **5**, 6652–6667.

10 B. Scrosati, J. Hassoun and Y. K. Sun, *Energy Environ. Sci.*, 2011, **4**, 3287–3295.

11 C.-X. Zu and H. Li, *Energy Environ. Sci.*, 2011, **4**, 2614–2624.

12 A. Zhamu, G. Chen, C. Liu, D. Neff, Q. Fang, Z. Yu, W. Xiong, Y. Wang, X. Wang and B. Z. Jang, *Energy Environ. Sci.*, 2012, **5**, 5701–5707.

13 H. Li, Z. Wang, L. Chen and X. Huang, *Adv. Mater.*, 2009, **21**, 4593–4607.

14 M. Winter and R. J. Brodd, *Chem. Rev.*, 2004, **104**, 4245–4269.

15 R. Dominko, D. Arcon, A. Mrzel, A. Zorko, P. Cevc, P. Venturini, M. Gaberscek, M. Remskar and D. Mihailovic, *Adv. Mater.*, 2002, **14**, 1531–1534.

16 C. M. Park, J. H. Kim, H. Kim and H. J. Sohn, *Chem. Soc. Rev.*, 2010, **39**, 3115–3141.

17 S. Brutti, V. Gentili, H. Menard, B. Scrosati and P. G. Bruce, *Adv. Energy Mater.*, 2012, **2**, 322–327.

18 J. Baker, *Energy Policy*, 2008, **36**, 4368–4373.

19 S. G. Chalka and J. F. Miller, *J. Power Sources*, 2006, **159**, 73–80.

20 J. B. Goodenough, *Energy Environ. Sci.*, 2014, **7**, 14–18.

21 K. Zaghiba, M. Dontignya, A. Guerfia, P. Charest, I. Rodrigues, A. Mauger and C. M. Julienc, *J. Power Sources*, 2011, **196**, 3949–3954.

22 F. Risacher and B. Fritz, *Aquat. Geochem.*, 2009, **15**, 123–157.

23 A. Yaksic and J. E. Tilton, *Resour. Policy*, 2009, **34**, 185–194.

24 P. Meister, H. Jia, J. Li, R. Kloepsch, M. Winter and T. Placke, *Chem. Mater.*, 2016, **28**, 7203–7217.

25 D. Kundu, E. Talaie, V. Duffort and L. F. Nazar, *Angew. Chem., Int. Ed.*, 2015, **54**, 3431–3448.

26 X. L. Hu, W. Zhang, X. X. Liu, Y. N. Mei and Y. H. Huang, *Chem. Soc. Rev.*, 2015, **44**, 2376–2404.

27 Y. C. Liu, Y. Li, H. Y. Kang, T. Jin and L. F. Jiao, *Mater. Horiz.*, 2016, **3**, 402–421.

28 Y. N. Mei, Y. H. Huang and X. L. Hu, *J. Mater. Chem. A*, 2016, **4**, 12001–12013.

29 L. L. Peng, Y. Zhu, D. H. Chen, R. S. Ruoff and G. H. Yu, *Adv. Energy Mater.*, 2016, **6**, 1600025.

30 W. Luo, F. Shen, C. Bommier, H. L. Zhu, X. L. Ji and L. B. Hu, *Acc. Chem. Res.*, 2016, **49**, 231–240.

31 G. H. Newman and L. P. Klemann, *J. Electrochem. Soc.*, 1980, **127**, 2097–2099.

32 C. Delmas, J.-J. Braconnier, C. Fouassier and P. Hagenmuller, *Solid State Ionics*, 1981, **3**, 165–169.

33 K. Mizushima, P. C. Jones, P. J. Wiseman and J. B. Goodenough, *Mater. Res. Bull.*, 1980, **15**, 783–798.

34 V. Palomares, P. Serras, I. Villaluenga, K. B. Hueso, J. Carretero-Gonzalez and T. Rojo, *Energy Environ. Sci.*, 2012, **5**, 5884–5901.

35 B. L. Ellis and L. F. Nazar, *Curr. Opin. Solid State Mater. Sci.*, 2012, **16**, 168–177.

36 M. D. Slater, D. Kim, E. Lee and C. S. Johnson, *Adv. Funct. Mater.*, 2013, **23**, 947–958.

37 F. Cheng, J. Liang, Z. Tao and J. Chen, *Adv. Mater.*, 2011, **23**, 1695–1715.

38 X. Xiang, K. Zhang and J. Chen, *Adv. Mater.*, 2015, **27**, 5343–5364.

39 V. L. Chevrier and G. Ceder, *J. Electrochem. Soc.*, 2011, **158**, A1011–A1014.

40 J. Ding, H. Wang, Z. Li, K. Cui, D. Karpuzov, X. Tan, A. Kohandehghan and D. Mitlin, *Energy Environ. Sci.*, 2015, **8**, 941–955.

41 N. Yabuuchi, K. Kubota, M. Dahbi and S. Komaba, *Chem. Rev.*, 2014, **114**, 11636–11682.

42 H. Pan, Y.-S. Hu and L. Chen, *Energy Environ. Sci.*, 2013, **6**, 2338–2360.

43 M. H. Han, E. Gonzalo, G. Singh and T. Rojo, *Energy Environ. Sci.*, 2015, **8**, 81–102.

44 H. Kang, Y. Liu, K. Cao, Y. Zhao, L. Jiao, Y. Wang and H. Yuan, *J. Mater. Chem. A*, 2015, **3**, 17899–17913.

45 L. P. Wang, L. Yu, X. Wang, M. Srinivasan and Z. J. Xu, *J. Mater. Chem. A*, 2015, **3**, 9353–9378.

46 I. A. Udod, H. B. Orman and V. K. Genchel, *Carbon*, 1994, **32**, 101–106.

47 M. M. Doeff, Y. Ma, S. J. Visco and L. C. De Jonghe, *J. Electrochem. Soc.*, 1993, **140**, L169–L170.

48 D. A. Stevens and J. R. Dahn, *J. Electrochem. Soc.*, 2000, **147**, 1271–1273.

49 D. Y. W. Yu, P. V. Prikhodchenko, C. W. Mason, S. K. Batabyal, J. Gun, S. Sladkevich, A. G. Medvedev and O. Lev, *Nat. Commun.*, 2013, **4**, 2922.

50 Z. M. Liu, X. Y. Yu, X. W. Lou and U. Paik, *Energy Environ. Sci.*, 2016, **9**, 2314–2318.

51 L. Wu, X. Hu, J. Qian, F. Pei, F. Wu, R. Mao, X. Ai, H. Yang and Y. Cao, *Energy Environ. Sci.*, 2014, **7**, 323–328.

52 Y. Xu, Y. Zhu, Y. Liu and C. Wang, *Adv. Energy Mater.*, 2013, **3**, 128–133.

53 L. Baggetto, J. K. Keum, J. F. Browning and G. M. Veith, *Electrochem. Commun.*, 2013, **34**, 41–44.

54 M. Gu, A. Kushima, Y. Shao, J.-G. Zhang, J. Liu, N. D. Browning, J. Li and C. Wang, *Nano Lett.*, 2013, **13**, 5203–5211.

55 S. Yuan, X.-L. Huang, D.-L. Ma, H.-G. Wang, F.-Z. Meng and X.-B. Zhang, *Adv. Mater.*, 2014, **26**, 2273–2279.

56 S. Zhang, X. Yu, H. Yu, Y. Chen, P. Gao, C. Li and C. Zhu, *ACS Appl. Mater. Interfaces*, 2014, **6**, 21880–21885.

57 Z. Jian, P. Liu, F. Li, M. Chen and H. Zhou, *J. Mater. Chem. A*, 2014, **2**, 13805–13809.

58 Z. Hu, Z. Zhu, F. Cheng, K. Zhang, J. Wang, C. Chen and J. Chen, *Energy Environ. Sci.*, 2015, **8**, 1309–1316.

59 S. Q. Wang, L. Xia, L. Yu, L. Zhang, H. H. Wang and X. W. Lou, *Adv. Energy Mater.*, 2016, **6**, 1502217.

60 K. Tang, L. Fu, R. J. White, L. Yu, M.-M. Titirici, M. Antonietti and J. Maier, *Adv. Energy Mater.*, 2012, **2**, 873–877.

61 S. Komaba, W. Murata, T. Ishikawa, N. Yabuuchi, T. Ozeki, T. Nakayama, A. Ogata, K. Gotoh and K. Fujiwara, *Adv. Funct. Mater.*, 2011, **21**, 3859–3867.

62 L. Zhao, J. Zhao, Y.-S. Hu, H. Li, Z. Zhou, M. Armand and L. Chen, *Adv. Energy Mater.*, 2012, **2**, 962–965.

63 Y. Park, D.-S. Shin, S. H. Woo, N. S. Choi, K. H. Shin, S. M. Oh, K. T. Lee and S. Y. Hong, *Adv. Mater.*, 2012, **24**, 3562–3567.

64 M. Li, S. Yu, Z. Chen, Z. Wang, F. Lv, B. Nan, Y. Zhu, Y. Shi, W. Wang, S. Wu, H. Liu, Y. Tang and Z. Lu, *Inorg. Chem. Front.*, 2017, **4**, 289–295.

65 A. Rudola, K. Saravanan, C. W. Masona and P. Balaya, *J. Mater. Chem. A*, 2013, **1**, 2653–2662.

66 H. Xiong, M. D. Slater, M. Balasubramanian, C. S. Johnson and T. Rajh, *J. Phys. Chem. Lett.*, 2011, **2**, 2560–2565.

67 X. Xu, S. Ji, M. Gu and J. Liu, *ACS Appl. Mater. Interfaces*, 2015, **7**, 20957–20964.

68 X. Liu, K. Zhang, K. Lei, F. Li, Z. Tao and J. Chen, *Nano Res.*, 2016, **9**, 198–206.

69 T. Wang, P. Hu, C. Zhang, H. Du, Z. Zhang, X. Wang, S. Chen, J. Xiong and G. Cui, *ACS Appl. Mater. Interfaces*, 2016, **8**, 7811–7817.

70 F. Klein, B. Jache, A. Bhide and P. Adelhelm, *Phys. Chem. Chem. Phys.*, 2013, **15**, 15876–15887.

71 J. Zhou, J. Qin, L. Guo, N. Zhao, C. Shi, E.-Z. Liu, F. He, L. Ma, J. Li and C. He, *J. Mater. Chem. A*, 2016, **4**, 17370–17380.

72 A. Samad, M. Noor-A-Alam and Y.-H. Shin, *J. Mater. Chem. A*, 2016, **4**, 14316–14323.

73 D. Chao, P. Liang, Z. Chen, L. Bai, H. Shen, X. Liu, X. Xia, Y. Zhao, S. V. Savilov, J. Lin and Z. X. Shen, *ACS Nano*, 2016, **10**, 10211–10219.

74 S. Z. Butler, S. M. Hollen, L. Cao, Y. Cui, J. A. Gupta, H. R. Gutiérrez, T. F. Heinz, S. S. Hong, J. Huang, A. F. Ismach, E. Johnston-Halperin, M. Kuno, V. V. Plashnitsa, R. D. Robinson, R. S. Ruoff, S. Salahuddin, J. Shan, L. Shi, M. G. Spencer, M. Terrones, W. Windl and J. E. Goldberger, *ACS Nano*, 2013, **7**, 2898–2926.

75 Q. H. Wang, K. Kalantar-Zadeh, A. Kis, J. N. Coleman and M. S. Strano, *Nat. Nanotechnol.*, 2012, **7**, 699–712.

76 H. Wang, H. Yuan, S. Sae Hong, Y. Li and Y. Cui, *Chem. Soc. Rev.*, 2015, **44**, 2664–2680.

77 B. Radisavljevic, A. Radenovic, J. Brivio, V. Giacometti and A. Kis, *Nat. Nanotechnol.*, 2011, **6**, 147–150.

78 S. Wu, S. Buckley, J. R. Schaibley, L. Feng, J. Yan, D. G. Mandrus, F. Hatami, W. Yao, J. Vuckovic, A. Majumdar and X. Xu, *Nature*, 2015, **520**, 69–72.

79 Y. Guo, K. Xu, C. Wu, J. Zhao and Y. Xie, *Chem. Soc. Rev.*, 2015, **44**, 637–646.

80 X. Peng, L. Peng, C. Wu and Y. Xie, *Chem. Soc. Rev.*, 2014, **43**, 3303–3323.

81 Y. Sun, S. Gao, F. Lei, C. Xiao and Y. Xie, *Acc. Chem. Res.*, 2015, **48**, 3–12.

82 J. Wu, H. Schmidt, K. K. Amara, X. Xu, G. Eda and B. Özyilmaz, *Nano Lett.*, 2014, **14**, 2730–2734.

This journal is © The Royal Society of Chemistry 2017

J. Mater. Chem. A, 2017, **5**, 7667–7690 | 7687

83 S. Tepavcevic, H. Xiong, V. R. Stamenkovic, X. Zuo, M. Balasubramanian, V. B. Prakapenka, C. S. Johnson and T. Rajh, *ACS Nano*, 2012, **6**, 530–538.

84 J. Huang, Z. Xu, L. Cao, Q. Zhang, H. Ouyang and J. Li, *Energy Technol.*, 2015, **3**, 1108–1114.

85 Y.-X. Wang, S.-L. Chou, D. Wexler, H.-K. Liu and S.-X. Dou, *Chem.–Eur. J.*, 2014, **20**, 9607–9612.

86 J. Park, J.-S. Kim, J. W. Park, T.-H. Nam, K. W. Kim, J. H. Ahn, G. Wang and H. J. Ahn, *Electrochim. Acta*, 2013, **92**, 427–432.

87 M. Mortazavi, C. Wang, J. Deng, V. B. Shenoy and N. V. Medhekar, *J. Power Sources*, 2014, **268**, 279–286.

88 X. Wang, X. Shen, Z. Wang, R. Yu and L. Chen, *ACS Nano*, 2014, **8**, 11394–11400.

89 P. Gao, L. Wang, Y. Zhang, Y. Huang and K. Liu, *ACS Nano*, 2015, **9**, 11296–11301.

90 S. D. Lacey, J. Wan, A. W. Cresce, S. M. Russell, J. Dai, W. Bao, K. Xu and L. Hu, *Nano Lett.*, 2015, **15**, 1018–1024.

91 W.-H. Ryu, J.-W. Jung, K. Park, S.-J. Kima and D. Kim, *Nanoscale*, 2014, **6**, 10975–10981.

92 D. Su, S. Dou and G. Wang, *Adv. Energy Mater.*, 2015, **5**, 1401205.

93 X. Wang, Y. Li, Z. Guan, Z. Wang and L. Chen, *Chem.–Eur. J.*, 2015, **21**, 6465–6468.

94 M. Xu, F. L. Yi, Y. Niu, J. Xie, J. Hou, S. Liu, W. H. Hu, Y. Li and C. M. Li, *J. Mater. Chem. A*, 2015, **3**, 9932–9937.

95 Z.-T. Shi, W. Kang, J. Xu, Y.-W. Sun, M. Jiang, T.-W. Ng, H.-T. Xue, D. Y. W. Yu, W. Zhang and C.-S. Lee, *Nano Energy*, 2016, **22**, 27–37.

96 Z. Hu, L. Wang, K. Zhang, J. Wang, F. Cheng, Z. Tao and J. Chen, *Angew. Chem., Int. Ed.*, 2014, **53**, 12794–12798.

97 Y.-L. Ding, P. Kopold, K. Hahn, P. A. van Aken, J. Maier and Y. Yu, *Adv. Mater.*, 2016, **28**, 7774–7782.

98 C. Zhu, X. Mu, P. A. van Aken, Y. Yu and J. Maier, *Angew. Chem., Int. Ed.*, 2014, **53**, 2152–2156.

99 G. Sook Bang, K. Woo Nam, J. Y. Kim, J. Shin, J. W. Choi and S.-Y. Choi, *ACS Appl. Mater. Interfaces*, 2014, **6**, 7084–7089.

100 S. Ding, D. Zhang, J. S. Chen and X. W. Lou, *Nanoscale*, 2012, **4**, 95–98.

101 L. Zhang, H. B. Wu, Y. Yan, X. Wang and X. W. Lou, *Energy Environ. Sci.*, 2014, **7**, 3302–3306.

102 M. Wang, G. Li, H. Xu, Y. Qian and J. Yang, *ACS Appl. Mater. Interfaces*, 2013, **5**, 1003–1008.

103 G. Li, X. Zeng, T. Zhang, W. Ma, W. Li and M. Wang, *CrystEngComm*, 2014, **16**, 10754–10759.

104 Y. Wang, L. Yu and X. W. Lou, *Angew. Chem., Int. Ed.*, 2016, **55**, 7423–7426.

105 J. Shuai, H. D. Yoo, Y. Liang, Y. Li, Y. Yao and L. C. Grabow, *Mater. Res. Express*, 2016, **3**, 064001.

106 X. Wang, Z. Guan, Y. Li, Z. Wang and L. Chen, *Nanoscale*, 2015, **7**, 637–641.

107 Y. Li, Y. Liang, F. C. Robles Hernandez, H. D. Yoa, Q. An and Y. Yao, *Nano Energy*, 2015, **15**, 453–461.

108 H. Liu, H. Hu, J. Wang, P. Niehoff, X. He, E. Pillard, D. Eder, M. Winter and J. Li, *Isr. J. Chem.*, 2015, **55**, 599–603.

109 Z.-T. Shi, W. Kang, J. Xu, L.-L. Sun, C. Wu, L. Wang, Y.-Q. Yu, D. Y. W. Yu, W. Zhang and C.-S. Lee, *Small*, 2015, **11**, 5667–5674.

110 J. Zhang, W. Kang, M. Jiang, Y. You, Y. Cao, T.-W. Ng, D. Y. W. Yu, C.-S. Lee and J. Xu, *Nanoscale*, 2017, **9**, 1484–1490.

111 Y.-X. Wang, K. H. Seng, S.-L. Chou, J.-Z. Wang, Z. Guo, D. Wexler, H.-K. Liu and S.-X. Dou, *Chem. Commun.*, 2014, **50**, 10730–10733.

112 J. Wang, C. Luo, T. Gao, A. Langrock, A. C. Mignerey and C. Wang, *Small*, 2015, **11**, 473–481.

113 X. Xu, D. Yu, H. Zhou, L. Zhang, C. Xiao, C. Guo, S. Guo and S. Ding, *J. Mater. Chem. A*, 2016, **4**, 4375–4379.

114 X. Zhang, X. Li, J. Liang, Y. Zhu and Y. Qian, *Small*, 2016, **12**, 2484–2491.

115 M. Li, Z. Wu, Z. Wang, S. Yu, Y. Zhu, B. Nan, Y. Shi, Y. Gu, H. Liu, Y. Tang and Z. Lu, *RSC Adv.*, 2017, **7**, 285–289.

116 Y. Wang, Q. Qu, G. Li, T. Gao, F. Qian, J. Shao, W. Liu, Q. Shi and H. Zheng, *Small*, 2016, **12**, 6033–6041.

117 Y. Lu, Q. Zhao, N. Zhang, K. Lei, F. Li and J. Chen, *Adv. Funct. Mater.*, 2016, **26**, 911–918.

118 X. Xiong, W. Luo, X. Hu, C. Chen, L. Qie, D. Hou and Y. Huang, *Sci. Rep.*, 2015, **5**, 9254.

119 X. Xie, T. Makaryan, M. Zhao, K. L. Van Aken, Y. Gogotsi and G. Wang, *Adv. Energy Mater.*, 2016, **6**, 1502161.

120 Y. Liu, X. He, D. Hanlon, A. Harvey, J. N. Coleman and Y. Li, *ACS Nano*, 2016, **10**, 8821–8828.

121 S. H. Choi, Y. N. Ko, J.-K. Lee and Y. C. Kang, *Adv. Funct. Mater.*, 2015, **25**, 1780–1788.

122 J. Xiang, D. Dong, F. Wen, J. Zhao, X. Zhang, L. Wang and Z. Liu, *J. Alloys Compd.*, 2016, **660**, 11–16.

123 X. Xie, Z. Ao, D. Su, J. Zhang and G. Wang, *Adv. Funct. Mater.*, 2015, **25**, 1393–1403.

124 L. David, R. Bhandavat and G. Singh, *ACS Nano*, 2014, **8**, 1759–1770.

125 W. Qin, T. Chen, L. Pan, L. Niu, B. Hua, D. Li, J. Li and Z. Sun, *Electrochim. Acta*, 2015, **153**, 55–61.

126 J. Wang, J. Liu, H. Yang, D. Chao, J. Yan, S. V. Savilove, J. Lin and Z. X. Shen, *Nano Energy*, 2016, **20**, 1–10.

127 S. H. Choi and Y. C. Kang, *ACS Appl. Mater. Interfaces*, 2015, **7**, 24694–24702.

128 B. Ahmed, D. H. Anjum, M. N. Hedhili and H. N. Alshareef, *Small*, 2015, **11**, 4341–4350.

129 J.-Y. Liao, B. D. Luna and A. Manthiram, *J. Mater. Chem. A*, 2016, **4**, 801–806.

130 G. Xu, L. Yang, X. Wei, J. Ding, J. Zhong and P. K. Chu, *Adv. Funct. Mater.*, 2016, **26**, 3349–3358.

131 S. Balendhran, S. Walia, H. Nili, J. Z. Ou, S. Zhuiykov, R. B. Kaner, S. Sriram, M. Bhaskaran and K. Kalantar-zadeh, *Adv. Funct. Mater.*, 2013, **23**, 3952–3970.

132 J. Morales, J. Santos and J. L. Tirado, *Solid State Ionics*, 1996, **83**, 57–64.

133 H. Wang, X. Lan, D. Jiang, Y. Zhang, H. Zhong, Z. Zhang and Y. Jiang, *J. Power Sources*, 2015, **283**, 187–194.

134 H. Wang, L. Wang, X. Wang, J. Quan, L. Mi, L. Yuan, G. Li, B. Zhang, H. Zhong and Y. Jiang, *J. Electrochem. Soc.*, 2016, **163**, A1627–A1632.

7688 | *J. Mater. Chem. A*, 2017, **5**, 7667–7690

This journal is © The Royal Society of Chemistry 2017

135 X. Yang, Z. Zhang, Y. Fu and Q. Li, *Nanoscale*, 2015, **7**, 10198–10203.

136 B. Wang, Y. Xia, G. Wang, Y. Zhou and H. Wang, *Chem. Eng. J.*, 2017, **309**, 417–425.

137 Y. N. Ko, S. H. Choi, S. B. Parkc and Y. C. Kang, *Nanoscale*, 2014, **6**, 10511–10515.

138 S. H. Choi and Y. C. Kang, *Nanoscale*, 2016, **8**, 4209–4216.

139 Z. Zhang, X. Yang, Y. Fu and K. Du, *J. Power Sources*, 2015, **296**, 2–9.

140 D. Xie, W. Tang, Y. Wang, X. Xia, Y. Zhong, D. Zhou, D. Wang, X. Wang and J. Tu, *Nano Res.*, 2016, **9**, 1618–1629.

141 Y. Zhang, Z. Liu, H. Zhao and Y. Du, *RSC Adv.*, 2016, **6**, 1440–1444.

142 J. S. Cho, H. S. Ju, J.-K. Lee and Y. C. Kang, *Nanoscale*, 2017, **9**, 1942–1950.

143 R. Chen, T. Zhao, W. Wu, F. Wu, L. Li, J. Qian, R. Xu, H. Wu, H. M. Albishri, A. S. Al-Bogami, D. A. El-Hady, J. Lu and K. Amine, *Nano Lett.*, 2014, **14**, 5899–5904.

144 D. Chen, G. Ji, B. Ding, Y. Ma, B. Qu, W. Chen and J. Y. Lee, *Nanoscale*, 2013, **5**, 7890–7896.

145 Y. Liu, N. Zhang, H. Kang, M. Shang, L. Jiao and J. Chen, *Chem.–Eur. J.*, 2015, **21**, 11878–11884.

146 D. Su, S. Dou and G. Wang, *Chem. Commun.*, 2014, **50**, 4192–4195.

147 S. H. Choi and Y. C. Kang, *Nanoscale*, 2015, **7**, 3965–3970.

148 C. Zhu, P. Kopold, W. Li, P. A. van Aken, J. Maier and Y. Yu, *J. Mater. Chem. A*, 2015, **3**, 20487–20493.

149 Y. Wang, D. Kong, W. Shi, B. Liu, G. J. Sim, Q. Ge and H. Y. Yang, *Adv. Energy Mater.*, 2016, **6**, 1601057.

150 W.-H. Ryu, H. Wilson, S. Sohn, J. Li, X. Tong, E. Shaulsky, J. Schroers, M. Elimelech and A. D. Taylor, *ACS Nano*, 2016, **10**, 3257–3266.

151 Z. Zhang, X. Yang and Y. Fu, *RSC Adv.*, 2016, **6**, 12726–12729.

152 Y. Liu, Y. Xu, Y. Zhu, J. N. Culver, C. A. Lundgren, K. Xu and C. Wang, *ACS Nano*, 2013, **7**, 3627–3634.

153 L. Wu, X. Hu, J. Qian, F. Pei, F. Wu, R. Mao, X. Ai, H. Yang and Y. Cao, *J. Mater. Chem. A*, 2013, **1**, 7181–7184.

154 D. Su, H.-J. Ahn and G. Wang, *Chem. Commun.*, 2013, **49**, 3131–3133.

155 D. Su, C. Wang, H. Ahn and G. Wang, *Phys. Chem. Chem. Phys.*, 2013, **15**, 12543–12550.

156 Y. Liu, N. Zhang, L. Jiao, Z. Tao and J. Chen, *Adv. Funct. Mater.*, 2015, **25**, 214–220.

157 Y.-X. Wang, Y.-G. Lim, M.-S. Park, S.-L. Chou, J. H. Kim, H.-K. Liu, S.-X. Dou and Y.-J. Kim, *J. Mater. Chem. A*, 2014, **2**, 529–534.

158 C. Zhu, P. Kopold, W. Li, P. A. van Aken, J. Maier and Y. Yu, *Adv. Sci.*, 2015, **2**, 1500200.

159 T. Zhou, W. K. Pang, C. Zhang, J. Yang, Z. Chen, H. K. Liu and Z. Guo, *ACS Nano*, 2014, **8**, 8323–8333.

160 B. Qu, C. Ma, G. Ji, C. Xu, J. Xu, Y. S. Meng, T. Wang and J. Y. Lee, *Adv. Mater.*, 2014, **26**, 3854–3859.

161 Y. Zhang, P. Zhu, L. Huang, J. Xie, S. Zhang, G. Cao and X. Zhao, *Adv. Funct. Mater.*, 2015, **25**, 481–489.

162 X. Xie, D. Su, S. Chen, J. Zhang, S. Dou and G. Wang, *Chem.–Asian J.*, 2014, **9**, 1611–1617.

163 S. H. Choi and Y. C. Kang, *Nano Res.*, 2015, **8**, 1595–1603.

164 Y. Liu, H. Kang, L. Jiao, C. Chen, K. Cao, Y. Wang and H. Yuan, *Nanoscale*, 2015, **7**, 1325–1332.

165 J. W. Seo, J. T. Jang, S. W. Park, C. J. Kim, B. W. Park and J. Cheon, *Adv. Mater.*, 2008, **20**, 4269–4273.

166 C. X. Zhai, N. Du, H. Zhang and D. R. Yang, *Chem. Commun.*, 2011, **47**, 1270–1272.

167 Y. P. Du, Z. Y. Yin, X. H. Rui, Z. Y. Zeng, X. J. Wu, J. Q. Liu, Y. Y. Zhu, J. X. Zhu, X. Huang, Q. Y. Yan and H. Zhang, *Nanoscale*, 2013, **5**, 1456–1459.

168 Q. Wu, L. F. Jiao, J. Du, J. Q. Yang, L. J. Guo, Y. C. Liu, Y. J. Wang and H. T. Yuan, *J. Power Sources*, 2013, **239**, 89–93.

169 W. Sun, X. Rui, D. Yang, Z. Sun, B. Li, W. Zhang, Y. Zong, S. Madhavi, S. Dou and Q. Yan, *ACS Nano*, 2015, **9**, 11371–11381.

170 B. Luo, Y. Fang, B. Wang, J. S. Zhou, H. H. Song and L. J. Zhi, *Energy Environ. Sci.*, 2012, **5**, 5226–5230.

171 L. Mei, C. Xu, T. Yang, J. M. Ma, L. B. Chen, Q. H. Li and T. H. Wang, *J. Mater. Chem. A*, 2013, **1**, 8658–8664.

172 G. C. Huang, T. Chen, W. X. Chen, Z. Wang, K. Chang, L. Ma, F. H. Huang, D. Y. Chen and J. Y. Lee, *Small*, 2013, **9**, 3693–3703.

173 K. Shiva, H. S. S. Ramakrishna Matte, H. B. Rajendraa, A. J. Bhattacharyyaa and C. N. R. Rao, *Nano Energy*, 2013, **2**, 787–793.

174 Y. Jiang, Y. Feng, B. Xi, S. Kai, K. Mi, J. Feng, J. Zhang and S. Xiong, *J. Mater. Chem. A*, 2016, **4**, 10719–10726.

175 Y. Jiang, M. Wei, J. Feng, Y. Ma and S. Xiong, *Energy Environ. Sci.*, 2016, **9**, 1430–1438.

176 J. Wang, C. Luo, J. Mao, Y. Zhu, X. Fan, T. Gao, A. C. Mignerey and C. Wang, *ACS Appl. Mater. Interfaces*, 2015, **7**, 11476–11481.

177 W. Xu, K. Zhao, L. Zhang, Z. Xie, Z. Cai and Y. Wang, *J. Alloys Compd.*, 2016, **654**, 357–362.

178 P. V. Prikhodchenko, D. Y. W. Yu, S. K. Batabyal, V. Uvarov, J. Gun, S. Sladkevich, A. A. Mikhaylov, A. G. Medvedevaf and O. Lev, *J. Mater. Chem. A*, 2014, **2**, 8431–8437.

179 H. Li, M. Zhou, W. Li, K. Wang, S. Cheng and K. Jiang, *RSC Adv.*, 2016, **6**, 35197–35202.

180 C. Ma, J. Xu, J. Alvarado, B. Qu, J. Somerville, J. Y. Lee and Y. S. Meng, *Chem. Mater.*, 2015, **27**, 5633–5640.

181 D. A. Winn, *Mater. Res. Bull.*, 1976, **11**, 559–566.

182 D. Tonti, C. Pettenkofer and W. Jaegermann, *Ionics*, 2000, **6**, 196–202.

183 D. Tonti, C. Pettenkofer and W. Jaegermann, *J. Phys. Chem. B*, 2004, **108**, 16093–16099.

184 H.-S. Ryu, J.-S. Kim, J.-S. Park, J.-W. Park, K.-W. Kim, J.-H. Ahn, T.-H. Nam, G. Wang and H.-J. Ahn, *J. Electrochem. Soc.*, 2013, **160**, A338–A343.

185 S. N. Li, J. B. Liu and B. X. Liu, *J. Power Sources*, 2016, **320**, 322–331.

186 Y. Liu, H. Wang, L. Cheng, N. Han, F. Zhao, P. Li, C. Jin and Y. Li, *Nano Energy*, 2016, **20**, 168–175.

187 J. Feng, X. Sun, C. Wu, L. Peng, C. Lin, S. Hu, J. Yang and Y. Xie, *J. Am. Chem. Soc.*, 2011, **133**, 17832–17838.

188 D. B. Putungan, S.-H. Lin and J.-L. Kuo, *ACS Appl. Mater. Interfaces*, 2016, **8**, 18754–18762.

189 J.-Y. Liao and A. Manthiram, *Nano Energy*, 2015, **18**, 20–27.

190 E. Yang, H. Ji and Y. Jung, *J. Phys. Chem. C*, 2015, **119**, 26374–26380.

191 Q. Zhang, S. Tan, R. G. Mendes, Z. Sun, Y. Chen, X. Kong, Y. Xue, M. H. Rümmeli, X. Wu, S. Chen and L. Fu, *Adv. Mater.*, 2016, **28**, 2616–2623.

192 Z. Hu, Z. Zhu, F. Cheng, K. Zhang, J. Wang, C. Chen and J. Chen, *Energy Environ. Sci.*, 2015, **8**, 1309–1316.

193 K. Zhang, M. Park, L. Zhou, G.-H. Lee, J. Shin, Z. Hu, S.-L. Chou, J. Chen and Y.-M. Kang, *Angew. Chem., Int. Ed.*, 2016, **55**, 12822–12826.

194 J. S. Cho, J.-K. Lee and Y. C. Kang, *Sci. Rep.*, 2016, **6**, 23699.

195 Z. Li, W. Feng, Y. Lin, X. Liu and H. Fei, *RSC Adv.*, 2016, **6**, 70632–70637.

196 Z. Shadike, M.-H. Cao, F. Ding, L. Sang and Z.-W. Fu, *Chem. Commun.*, 2015, **51**, 10486–10489.

197 K. Zhang, M. Park, L. Zhou, G.-H. Lee, W. Li, Y.-M. Kang and J. Chen, *Adv. Funct. Mater.*, 2016, **26**, 6728–6735.

198 T. Wang, P. Hu, C. Zhang, H. Du, Z. Zhang, X. Wang, S. Chen, J. Xiong and G. Cui, *ACS Appl. Mater. Interfaces*, 2016, **8**, 7811–7817.

199 J. S. Cho, S. Y. Lee and Y. C. Kang, *Sci. Rep.*, 2016, **6**, 23338.